

**UNCLASSIFIED**

**AD NUMBER**

**AD813107**

**LIMITATION CHANGES**

**TO:**

**Approved for public release; distribution is unlimited.**

**FROM:**

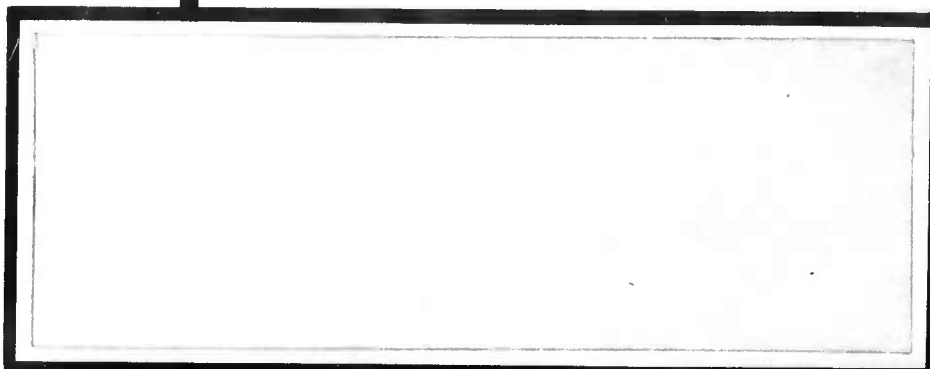
**Distribution authorized to U.S. Gov't. agencies and their contractors; Critical Technology; 28 FEB 1967. Other requests shall be referred to Air Force Technical Applications Center, Washington, DC 20333. This document contains export-controlled technical data.**

**AUTHORITY**

**USAF ltr dtd 25 Jan 1972**

**THIS PAGE IS UNCLASSIFIED**

AD 813107

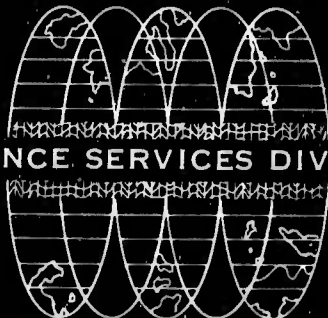


STATEMENT #2 UNCLASSIFIED

This document is subject to special export controls and each  
government or foreign national may  
make only with prior approval of AETAC - Vela Seismological Center  
Wash. DC



SCIENCE SERVICES DIVISION



TEXAS INSTRUMENTS  
INCORPORATED

TELECOMMUNICATIONS  
POWER SYSTEMS AND ELECTRONICS



AFTAC Project VT/4053

ARRAY RESEARCH  
ANALYSIS OF K-LINE WAVENUMBER SPECTRA  
FROM THE TFO LONG NOISE SAMPLE

Special Report No. 23

Prepared by  
John P. Burg, Project Scientist

Program Manager  
George C. Burrell

TEXAS INSTRUMENTS INCORPORATED  
Science Services Division  
P.O. Box 5621  
Dallas, Texas 75222

Contract No. AF 33(657)-12747  
Date of Contract: 13 November 1963  
Contract Expiration Date: 20 January 1967

Prepared for  
AIR FORCE TECHNICAL APPLICATIONS CENTER  
VELA Seismological Center  
Washington, D.C. 20333

ARPA Order No. 104-60

Project Code No. 8100

28 February 1967

---

science services division



## TABLE OF CONTENTS

Section	Title	Page
I	INTRODUCTION	1
II	DATA PREPARATION	3
III	DESCRIPTION OF THE K-LINE WAVENUMBER SPECTRA PLOTS	7
IV	GENERAL FEATURES OF THE K-LINE WAVENUMBER SPECTRA	23
V	THE NONSEISMICALLY INTERPRETABLE NOISE	27
VI	MANTLE P-WAVE NOISE	29
VII	RAYLEIGH WAVE NOISE	33
VIII	LINE SPECTRA	37
IX	PROPERTIES OF THE NEW WAVENUMBER SPECTRAL ESTIMATION TECHNIQUE	41
X	REFERENCES	59/60

## LIST OF ILLUSTRATIONS

Figure	Description	Page
1	Array at Tonto Forest Seismological Observatory (TFO)	4
2	Combined Frequency Response of the Prewhitenning Filter, the Bandpass Filter and the Deconvolution Filter	4
3	Response of the J-M Data PTA Seismometer System Used at TFO	4
4	Power Spectra of Z62, Z13, Z73, Z65 and Z70 After Deconvolution	4
5	Relative Amplitude of Bartlett Window vs Frequency in cps	5
6	21-Seismometer Averaged Absolute Power Density Spectra	6
7	Wavenumber and Integrated Spectra From the Two TFO Arms at Frequencies of 0.07528, 0.15056, 0.22584, and 0.30112 cps	9/10



---

## LIST OF ILLUSTRATIONS (Contd)

Figure	Description	Page
8	Wavenumber and Integrated Spectra From the Two TFO Arms at Frequencies of 0.37640, 0.45168, 0.52696, and 0.60224 cps	11/12
9	Wavenumber and Integrated Spectra From the Two TFO Arms at Frequencies at 0.67752, 0.75280, 0.82808, and 0.90336 cps	13/14
10	Wavenumber and Integrated Spectra From the Two TFO Arms at Frequencies of 0.97864, 1.0539, 1.1292, and 1.2045 cps	15/16
11	Wavenumber and Integrated Spectra From the Two TFO Arms at Frequencies of 1.2798, 1.3550, 1.4303, and 1.5056 cps	17/18
12	Wavenumber and Integrated Spectra From the Two TFO Arms at Frequencies of 1.5809, 1.6562, 1.7314, and 1.8067 cps	19/20
13	Fractional Prediction Error in db vs Frequency For Predicting One Seismometer Ahead Using a Line of Ten Seismometers	21/22
14	Surface Weather Map at 0600 GMT (12-20-63)	24
15	Absolute Frequency Power Spectra in db vs cps For Various Noise Components in the TFO Long Noise Sample	26
16	Estimated Vector Velocities of the Two Mantle P-Wave Peaks as a Function of Frequency	30
17	Estimated Surface Locations of the Mantle P-Wave Energy	31/32
18	Wavenumber and Integrated Spectra From the Two TFO Arms at the Frequency of 0.18820 cps	34
19	Estimated Velocity of the Rayleigh Wave at TFO as a Function of Frequency	36
20	Wavenumber and Integrated Spectra From the Two TFO Arms at the Frequencies of 1.6185 cps (above) and 2.0702 cps (below)	38
21	Comparison of the New Wavenumber Estimation Technique with More Conventional Techniques	43/44



---

## LIST OF ILLUSTRATIONS (Contd)

Figure	Description	Page
22	Approximations of the K/4 Fixed Speed, Isotropic Model as a Function of the Number of Seismometers	45
23	Approximations of the K/2 Fixed Speed, Isotropic Model as a Function of the Number of Seismometers	46
24	Approximations of the K/4 Solid Disk Model as a Function of the Number of Seismometers	47
25	Approximations of the K/2 Solid Disk Model as a Function of the Number of Seismometers	48
26	Approximations of the TFO 0.37640 cps Model as a Function of the Number of Seismometers	49
27	Approximations of the TFO 0.75280 cps Model as a Function of the Number of Seismometers	50
28	Comparison of Wavenumber Spectra at 0.37640 cps and 0.75280 cps with Theoretical Models	53
29	Estimated Wavenumber Spectra at 0.15056 cps as a Function of the Number of Seismometers	54
30	Estimated Wavenumber Spectra at 0.37640 cps as a Function of the Number of Seismometers	55
31	Estimated Wavenumber Spectra at 0.75280 cps as a Function of the Number of Seismometers	56
32	Estimated Wavenumber Spectra at 1.1292 cps as a Function of the Number of Seismometers	57/58



---

## SECTION I

### INTRODUCTION

This report contains the analysis of 1-dimensional wavenumber spectra obtained from a 20-min ambient seismic noise recording at a Tonto Forest Seismological Observatory crossarray. The history and past processing of this noise sample, known as the TFO long noise sample,<sup>1,2,3</sup> have been reported in three previous reports.

The 1-dimensional wavenumber spectra presented in this report are physically interpreted as projections of 2-dimensional power density spectra<sup>2</sup> onto perpendicular axes which are parallel to the two arms of the crossarray at TFO (Figure 1 gives the TFO geometry). Thus, these new wavenumber spectra give the power density of the ambient seismic noise as a function of its apparent wavenumber along each of the two arms of the array. Although knowledge of the spectral projections onto two perpendicular lines is basically inferior to knowing the 2-dimensional spectrum itself, the exceptionally high resolution of these K-line spectra allows a much finer analysis of the TFO long noise sample than could be done before using only the low resolution 2-dimensional spectra.

The basic input data for calculating each of these 1-dimensional wavenumber spectra is the crosspower matrix  $[\Phi_{ij}(f)]$ ; where  $f$  is frequency and  $i$  and  $j$  range over the 11 seismometers in one line of the array. The data processing leading to these crosspower matrices is discussed in Section II.

The major results of the analysis of these spectra are

- Agreement with and a higher resolution explanation of essentially all of the previous analyses of this noise data



---

- The quantitative separation of mantle P-wave noise, Rayleigh wave energy and nonseismically interpretable noise, allowing absolute frequency spectra to be estimated for each type
- The first clear proof of isotropic Rayleigh wave noise, together with an estimate of the velocity of this energy as a function of frequency
- Spectra and inelastic attenuation estimates for the Rayleigh wave coming across the North American continent from Newfoundland and for Rayleigh wave energy coming from the nearby Pacific Ocean
- Separation of the two storm generated mantle P-wave peaks for frequencies of 0.4 cps and above



---

## SECTION II

### DATA PREPARATION

The complete processing history of this noise sample has been previously reported.<sup>1, 2, 3</sup> However, a summary of the absolute power spectra analysis and the data processing leading to the crosspower spectra matrices is given here for the reader's convenience.

Absolute frequency power spectra for the TFO long noise sample were obtained from analysis of calibration data<sup>1</sup> and from the frequency response of the JM-PTA system used at TFO (Figure 2). Figure 3 shows the total digital filtering response later applied to the recorded data while it was being whitened and decimated down to a 216-msec sampling period. High resolution frequency power spectra for five particular channels after this filtering are shown in Figure 4. These absolute spectra indicate that at 1 cps the power density spectra for this noise sample is about 14.5 db down, relative to  $1 \text{ (m}\mu\text{)}^2/\text{cps}$ .

In Special Report No. 17,<sup>2</sup> spectral estimates of the noise sample were obtained by Bartlett smoothing and Fourier transforming the auto- and crosscorrelation functions discussed in Semiannual Technical Report No. 3.<sup>1</sup> These correlations, which go to  $\tau = \pm 61$ , were previously normalized so that the zero lags of the autocorrelations were unity. The auto- and crosspower matrices used in calculating the 1-dimensional spectra shown in this report were renormalized so that the main diagonal of the matrix was unity. (This was also the case for matrices discussed in Special Report No. 17.) Special Report No. 17 contains a minor error in the mathematical expression for the equivalent frequency convolution operator for the Bartlett weighting function. Figure 5 shows the correct formula and a plot of this Bartlett window. The bandwidth of this window is narrow

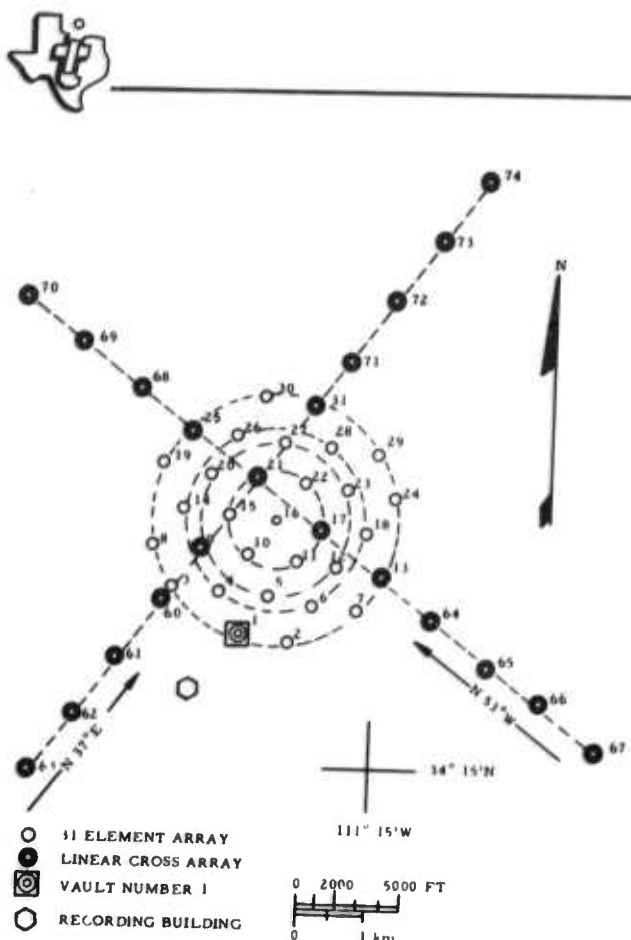


**Figure 1.** Array at Tonto Forest Seismological Observatory (TFO)

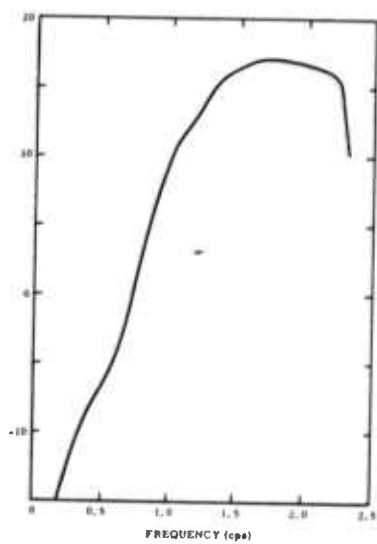


**Figure 2.** Combined Frequency Response of the Prewitthing Filter, the Bandpass Filter and the Deconvolution Filter

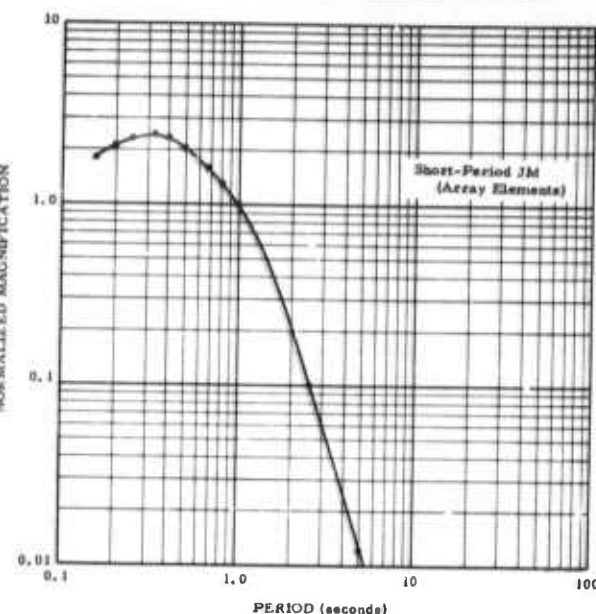


**Figure 3.** Response of the J-M Data PTA Seismometer System Used at TFO

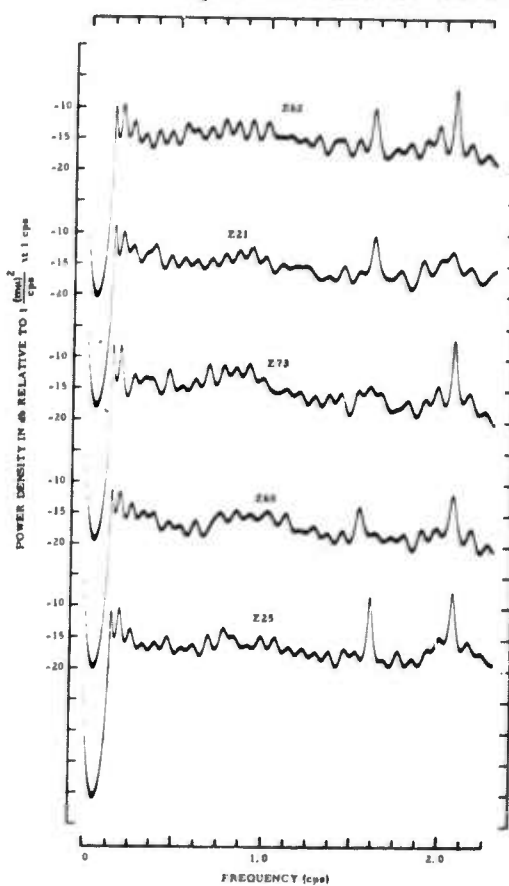


**Figure 4.** Power Spectra of Z62, Z13, Z73, Z65 and Z70 After Deconvolution



enough so that the wavenumber spectra were, given at frequencies separated by a  $\Delta f$  of 0.07528 cps, are essentially independent except for some leakage occurring at the lowest frequencies.

Using the average of the Bartlett smoothed power spectra from the 21 seismometers in the crossarray and the response curves in Figures 2 and 3, absolute frequency power density spectra for the TFO long noise sample for the various filter responses were calculated and are shown in Figure 6. It should be noted that all the curves were made to go through -14.5 db at 1 cps for this noise sample.

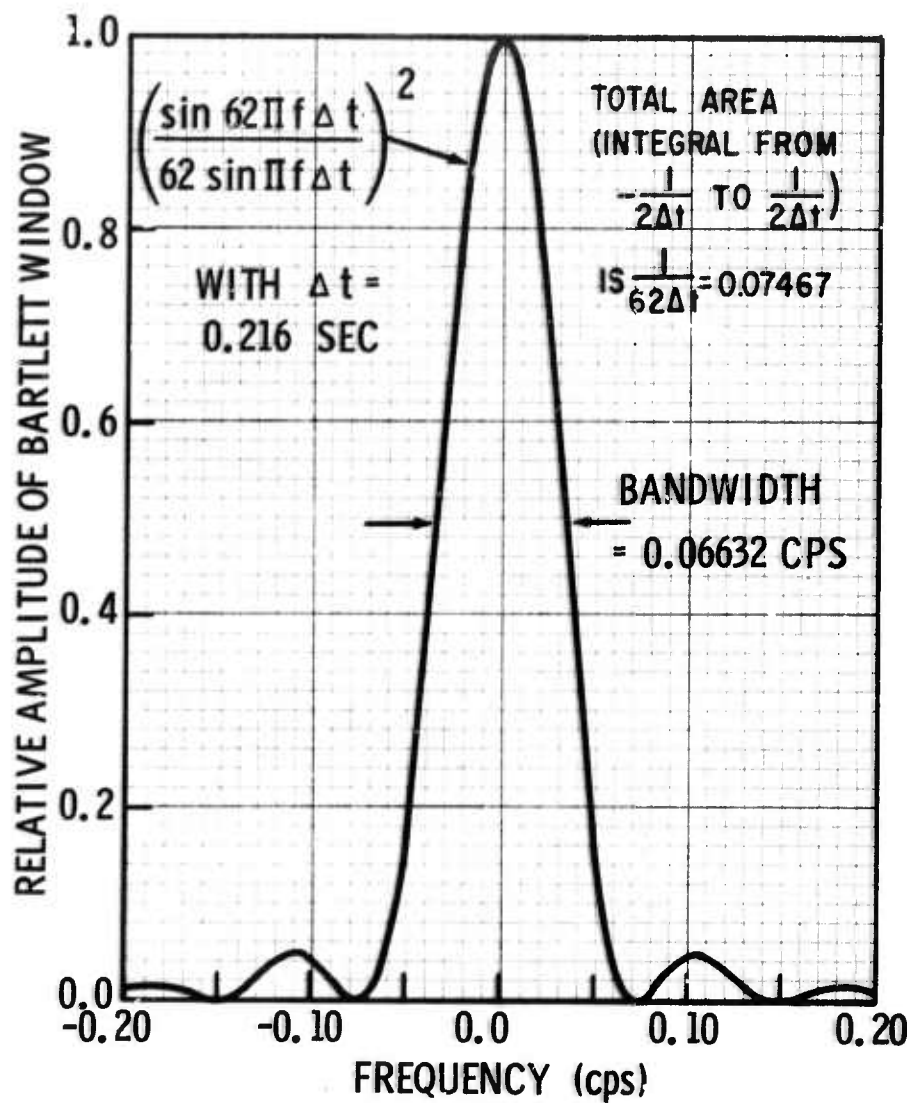


Figure 5. Relative Amplitude of Bartlett Window vs Frequency in cps

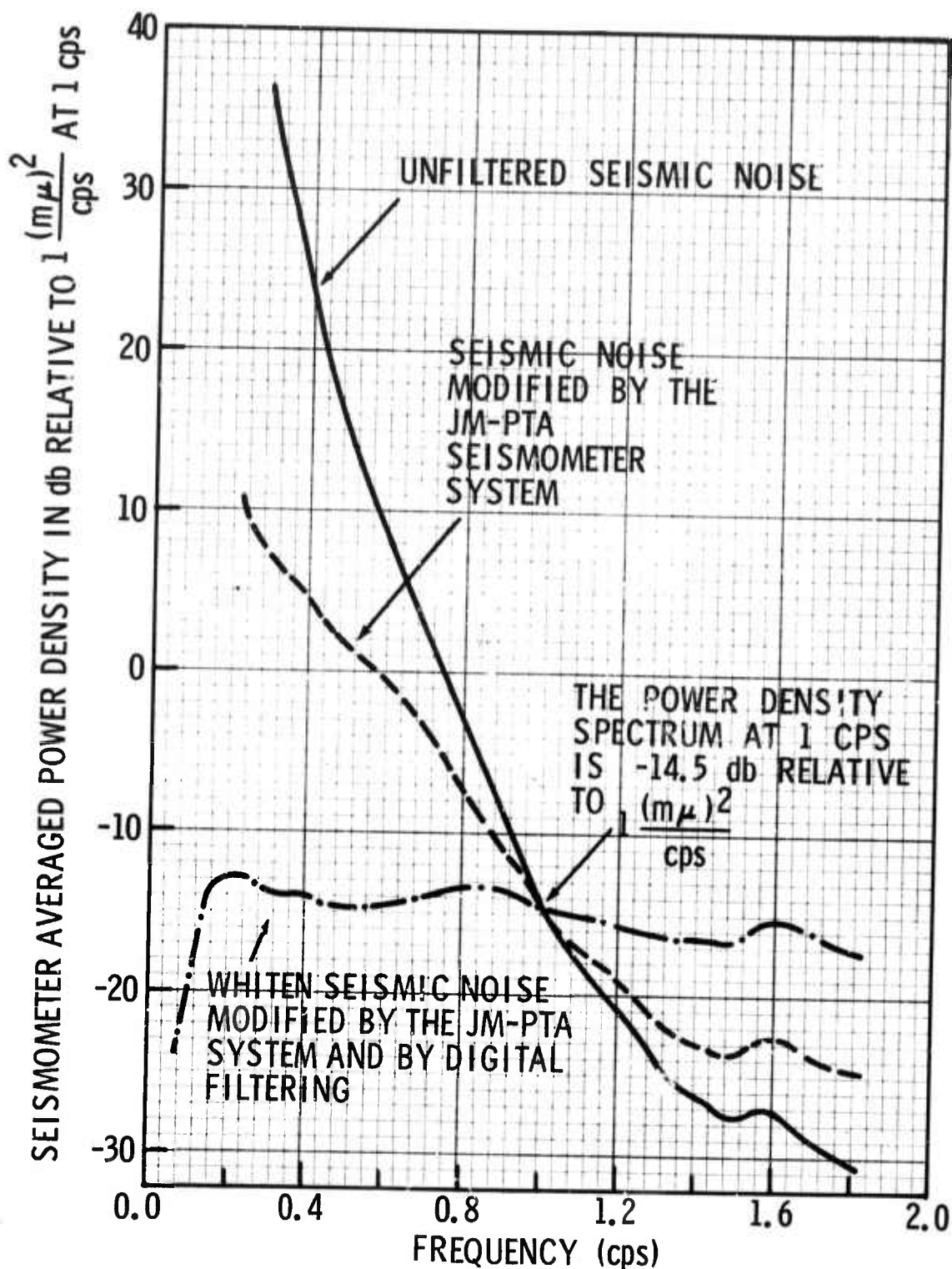


Figure 6. 21-Seismometer Averaged Absolute Power Density Spectra



### SECTION III

#### DESCRIPTION OF THE K-LINE WAVENUMBER SPECTRA PLOTS

The basic wavenumber spectra data, which make up the heart of this report, are shown in Figures 7 through 12. These spectra were obtained at 24 frequencies, starting with 0.07528 cps with increments of 0.07528 cps up to 1.8067 cps. For each frequency, there is a wavenumber power density spectrum and an integrated wavenumber power density function for each line of the TFO array (Figure 1).

For each of the wavenumber spectra (plotted in db vs wavenumber in cycles/km) the 0-db level indicates the average value of the spectrum. Thus, absolute wavenumber spectra can be calculated through use of the absolute frequency spectra given in Figure 6. The fold-over wavenumber value for the S37°W to N37°E line is 0.4706 cycles/km, and 0.4709 cycles/km is the value for the S53°E to N53°W line. These values are equal to one divided by two times the average spacing between seismometers along the two respective lines of the array. (The average spacing between seismometers is slightly more than 1 km.) In these wavenumber plots, the solid vertical line at  $k=0$  represents infinite apparent velocity along the arm of the array; i.e., the wave propagation is perpendicular to the arm. On either side of this line are dashed lines showing velocities of 8 km/sec and 3 km/sec. These two velocities are important as they are approximately the minimum apparent velocities for P-wave and Rayleigh-wave noise when the noise propagation is inline with an arm. Note that the 3 km/sec lines move off the figures after the 1.3550 cps plot. These wavenumber spectra are oriented so that power density on the right half of the plot represents energy coming from  $N37^{\circ}E \pm 90^{\circ}$  for the S37°W to N37°E line and energy coming from  $N53^{\circ}W \pm 90^{\circ}$  for the S53°E to N53°W line.



The normalized, integrated wavenumber power density function is

$$\int_{-K}^k P(k) dk, \quad \text{with } \int_{-K}^K P(k) dk = 1$$

where  $P(k)$  is the wavenumber power density spectrum and  $K$  is the foldover wavenumber. This function has been plotted in fractional power vs velocity in km/sec for those frequencies below 1.2045 cps. For 1.2045 cps and above, the abscissa changes to wavenumber in cycles/km. These integrated spectra are particularly useful plots in that they make it easy to measure the amount of power in any given velocity or wavenumber band.

To save space, a discrete function marked by small x's appears superimposed on these integrated spectrum plots. These x's show the fractional power that is unpredictable when one tries to predict the output of the next seismometer in line from a line of seismometers. In particular, the x on the right-hand edge is the fractional mean-square-error in predicting one seismometer ahead (about 1 km), using 10 seismometers in a line. The first x to the left of the edge is the prediction error, using only nine seismometers. This continues to the first x to the right of the left-hand edge which shows the prediction error using only one seismometer. The fractional prediction error in decibels, as a function of frequency for the two arms when 10 seismometers are used, is given in Figure 13. These prediction error curves show that the ambient seismic noise is almost spatially uncorrelated above 1.2 cps. The dip at 1.6 cps is due to correlated line spectra which can easily be seen in Figure 4.

WAVENUMBER POWER SPECTRA FROM THE S $37^{\circ}$ W - N $37^{\circ}$ E ARM IN dB VS CYCLES/KM

INTEGRATED FRACTIONAL POWER FROM THE S $37^{\circ}$ W - N $37^{\circ}$ E ARM VS VELOCITY IN KM/SEC

WAVENUMBER POWER SPECTRA FROM THE S $53^{\circ}$ E - N $53^{\circ}$ W ARM IN dB VS CYCLES/KM

INTEGRATED FRACTIONAL POWER FROM THE S $53^{\circ}$ E - N $53^{\circ}$ W ARM VS VELOCITY IN KM/SEC

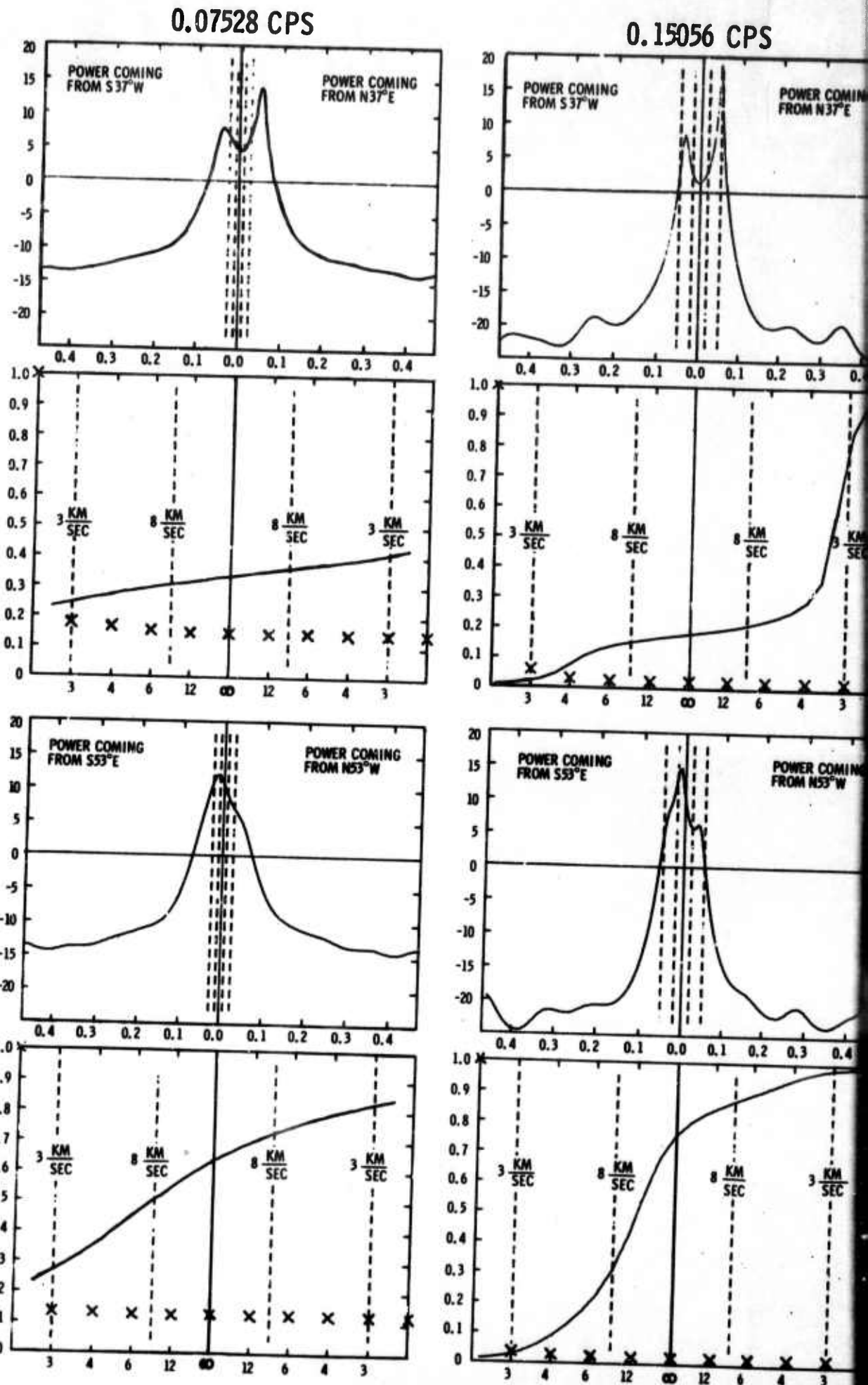
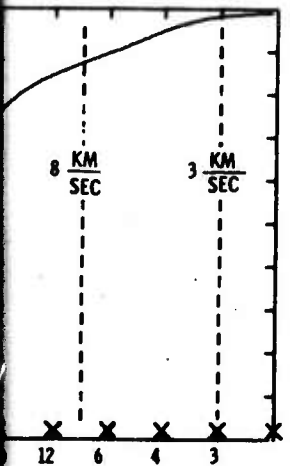
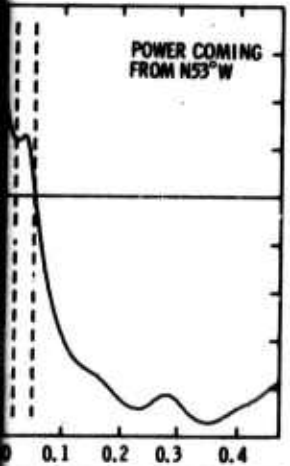
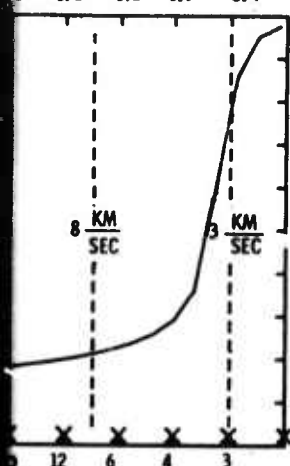
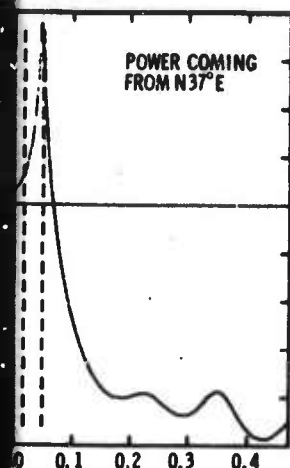
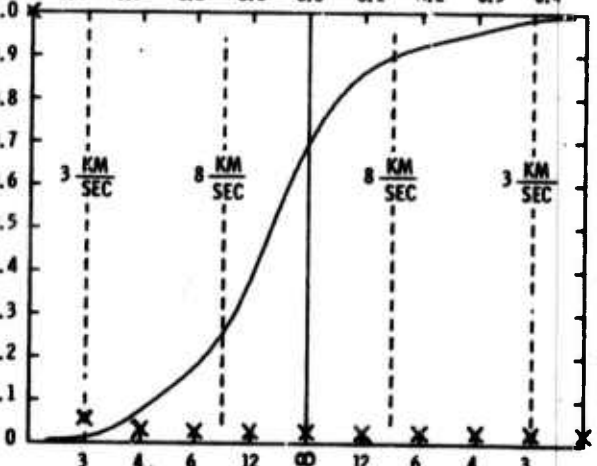
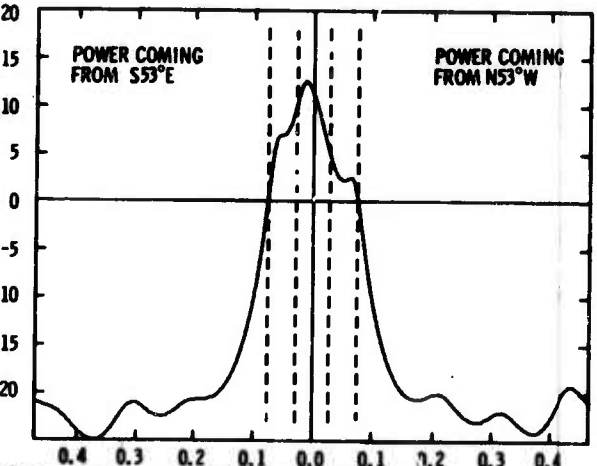
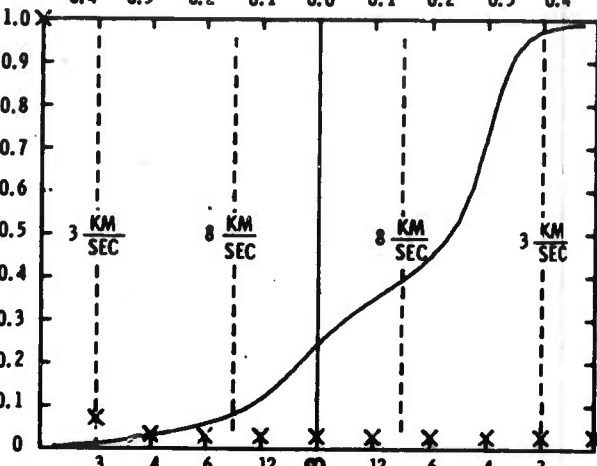
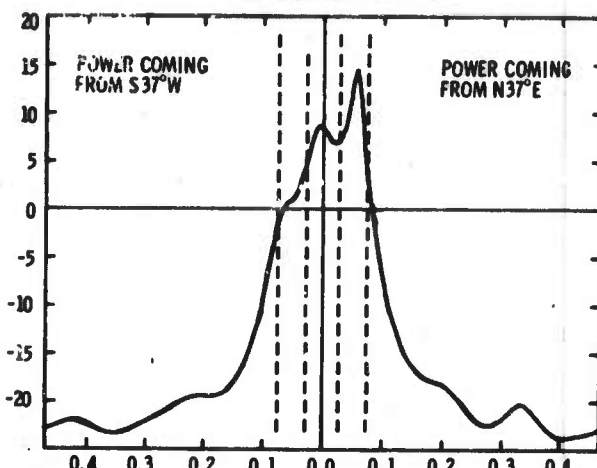


Figure 7. Wavenumber and Integrated Spectra From the Two TFO Arms at Frequencies 0.07528 CPS and 0.15056 CPS.

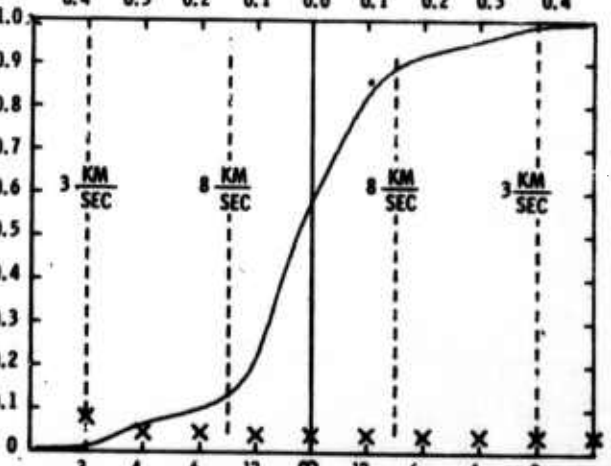
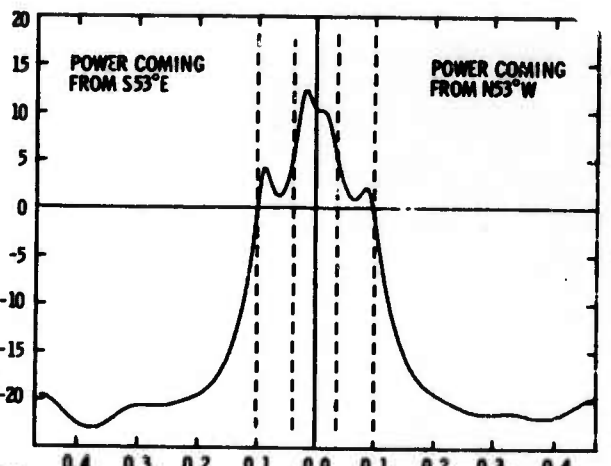
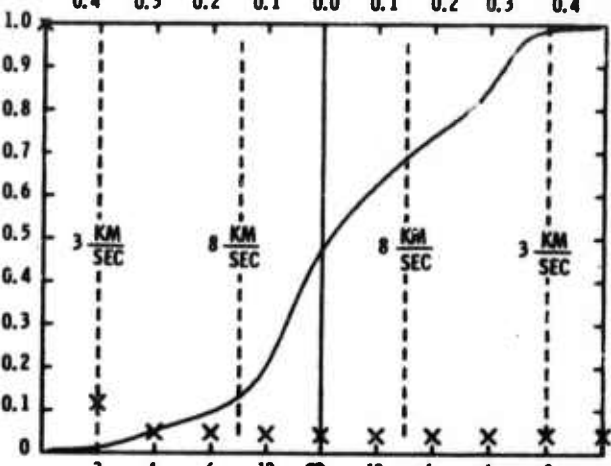
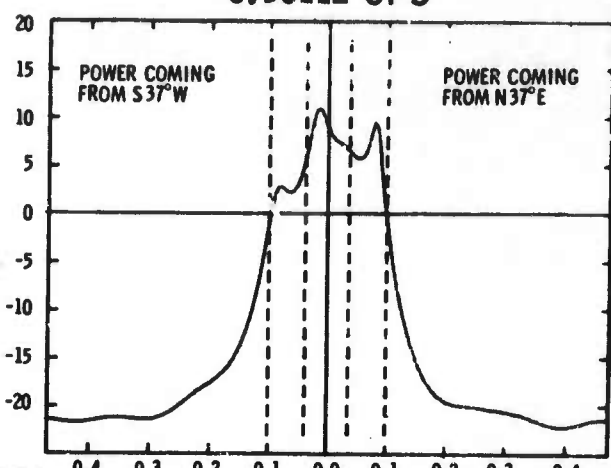
6 CPS



0.22584 CPS



0.30112 CPS

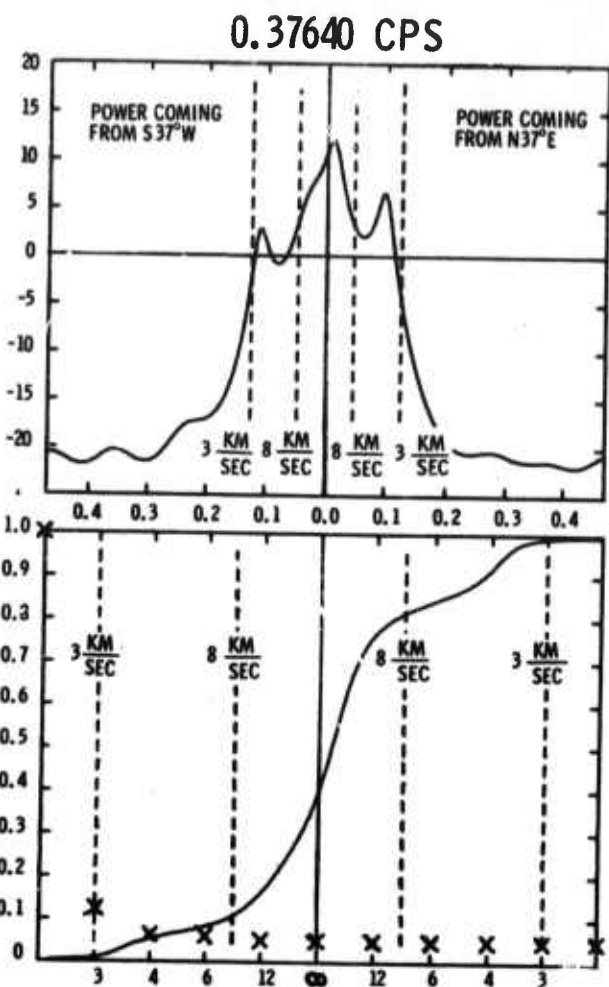


Arms at Frequencies of 0.07528, 0.15056, 0.22584, and 0.30112 cps

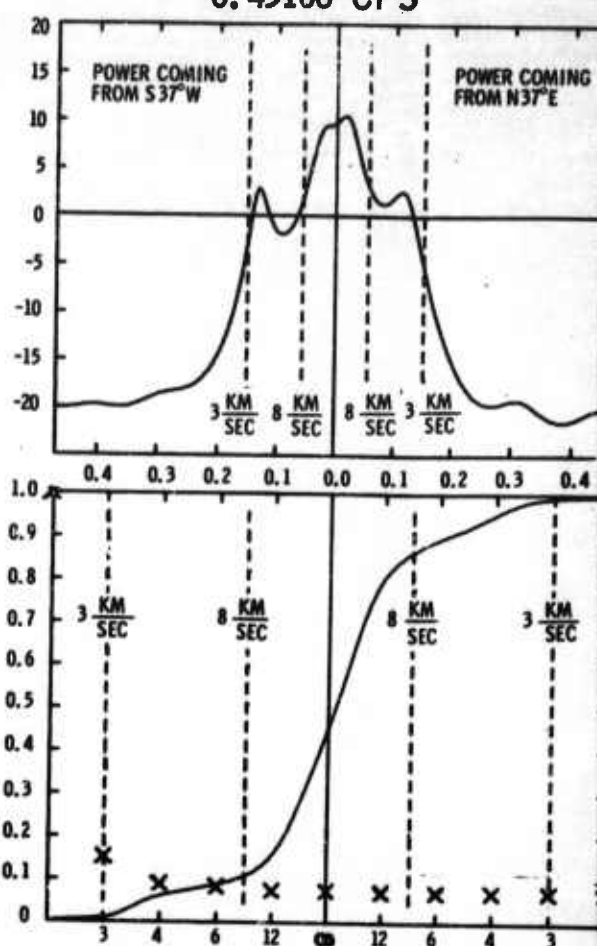
9/10

J

WAVENUMBER POWER SPECTRA FROM THE S37°W - N37°E ARM IN db VS CYCLES/KM



0.45168 CPS



WAVENUMBER POWER SPECTRA FROM THE S53°E - N53°W ARM IN db VS CYCLES/KM

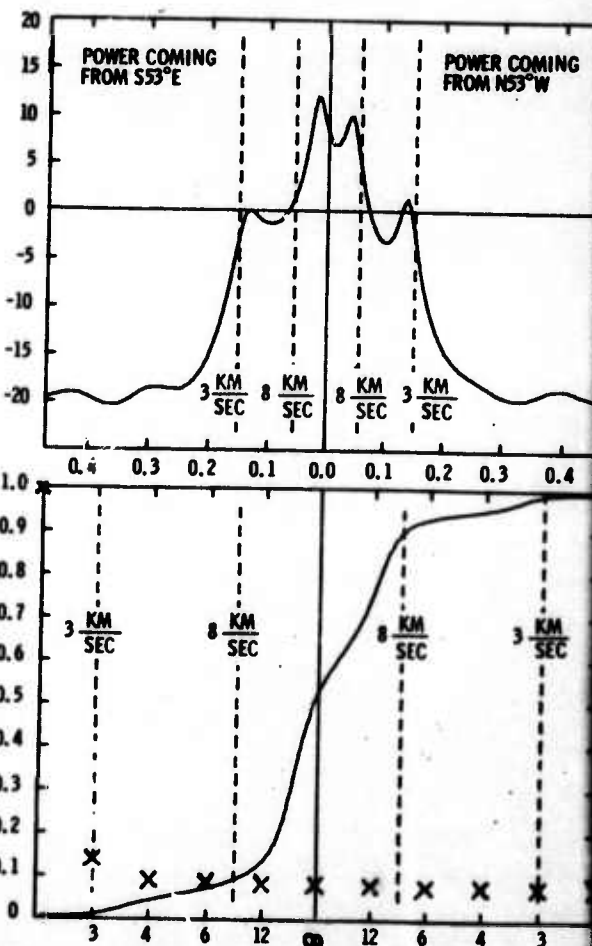
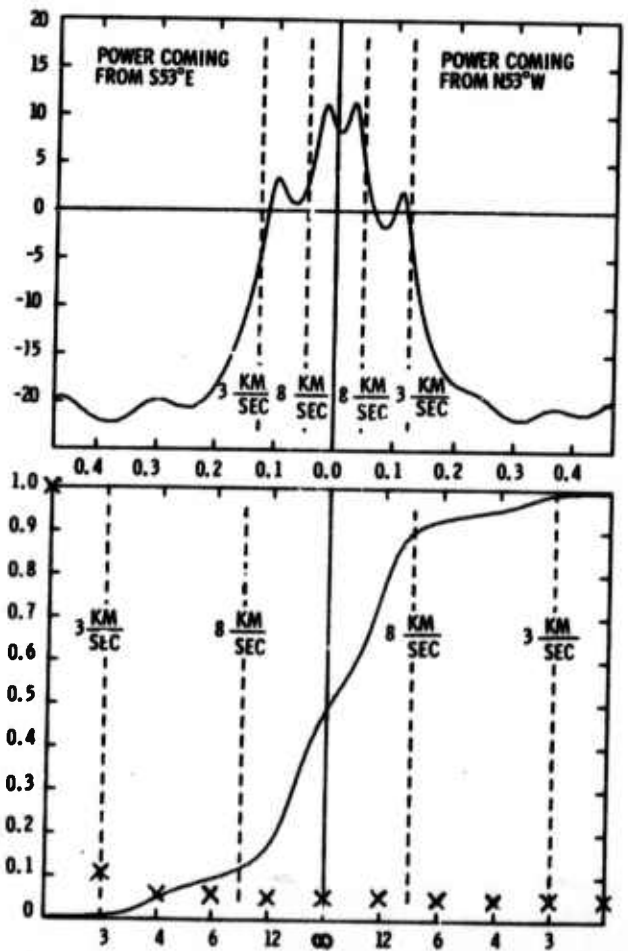
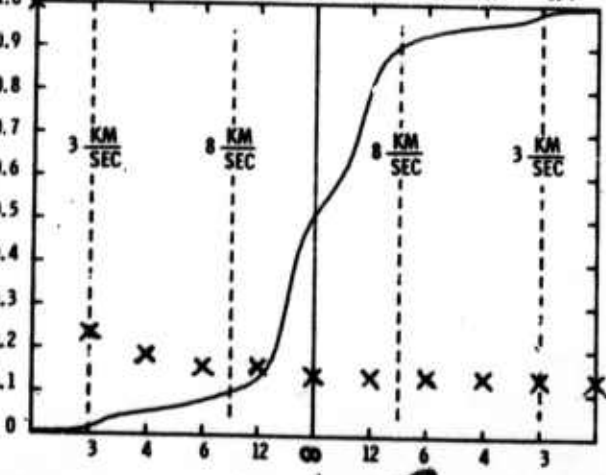
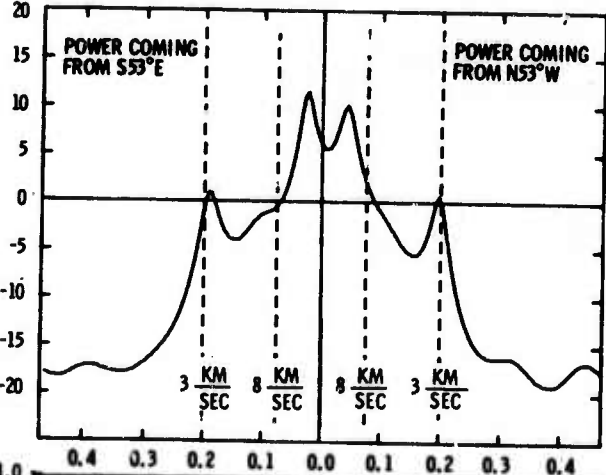
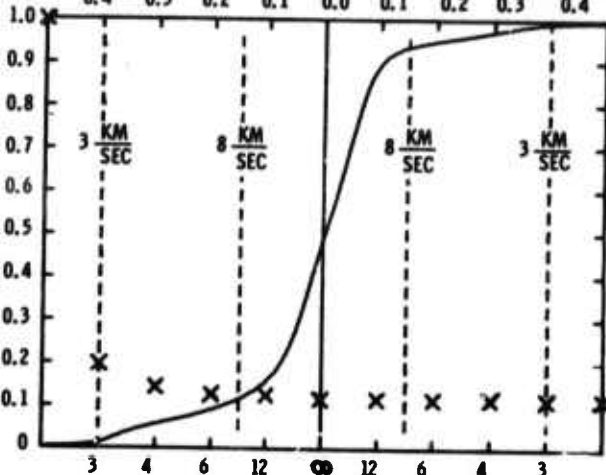
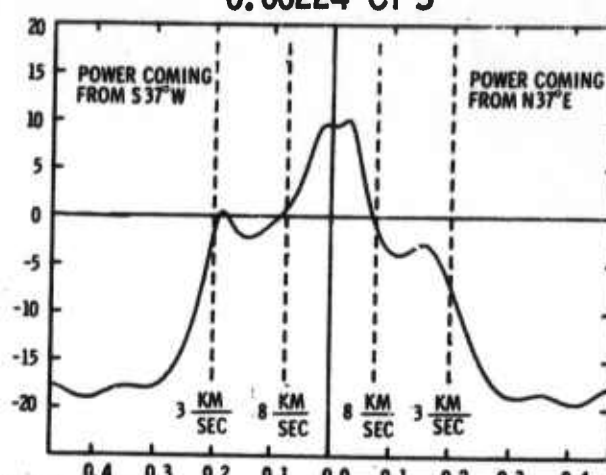
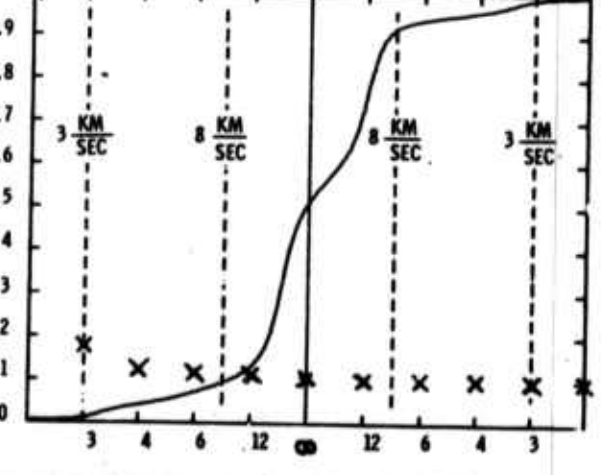
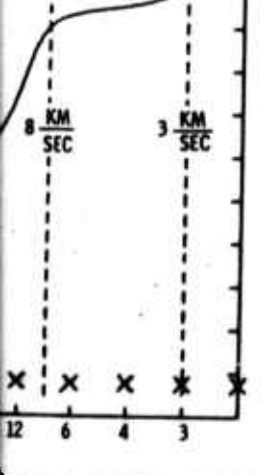
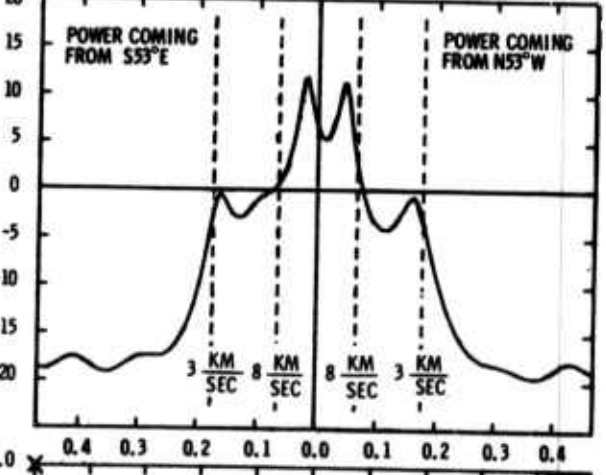
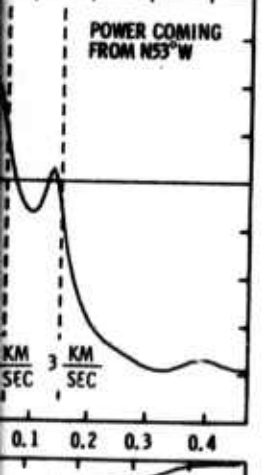
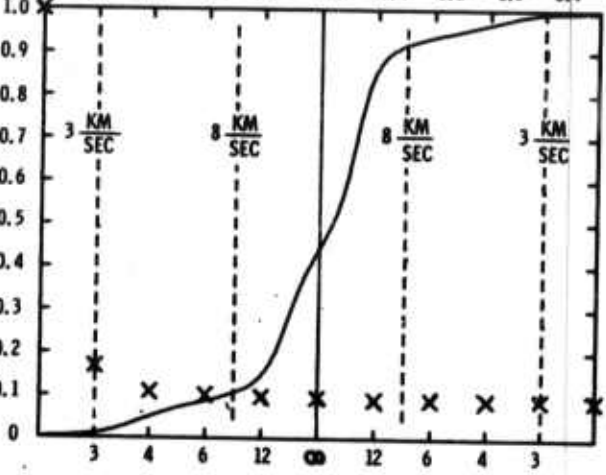
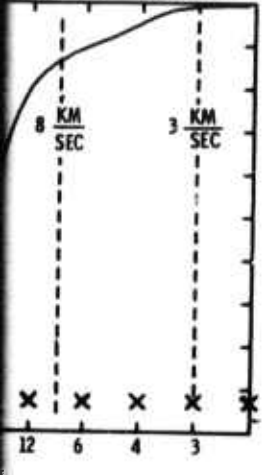
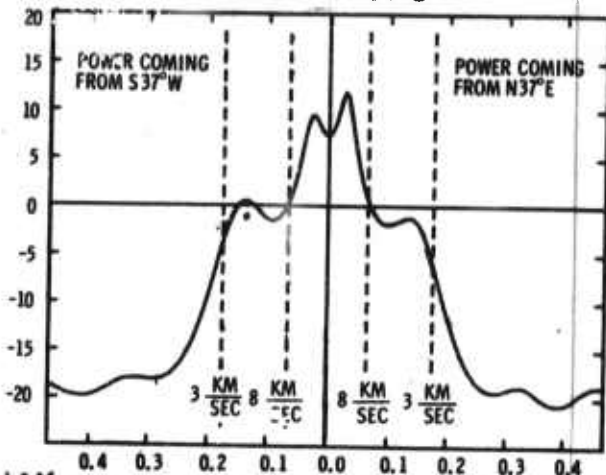
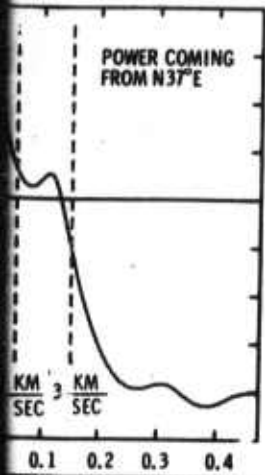


Figure 8. Wavenumber and Integrated Spectra From the Two TFO Arms at Frequencies 0.37640 CPS and 0.45168 CPS.

CPS

0.52696 CPS

0.60224 CPS

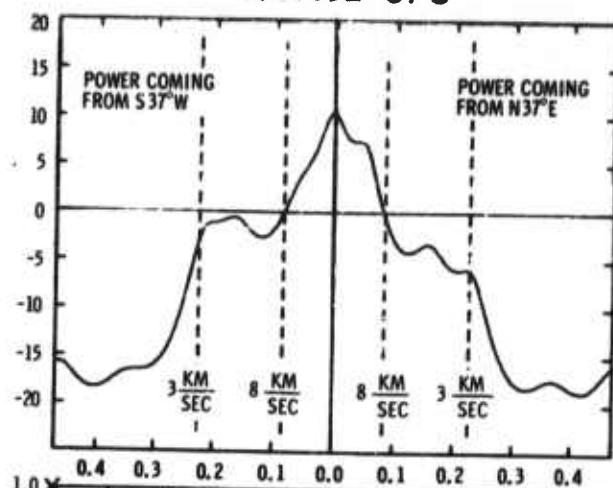


Arms at Frequencies of 0.37640, 0.45168, 0.52696, and 0.60224 cps

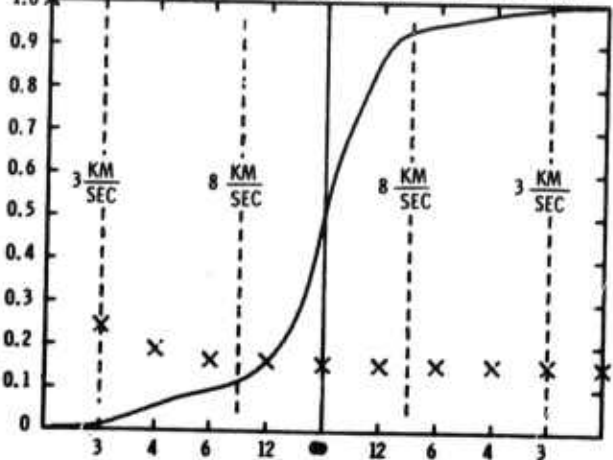
11/12

WAVENUMBER POWER SPECTRA FROM THE S $37^{\circ}$ W - N $37^{\circ}$ E ARM IN db VS CYCLES/KM

0.67752 CPS

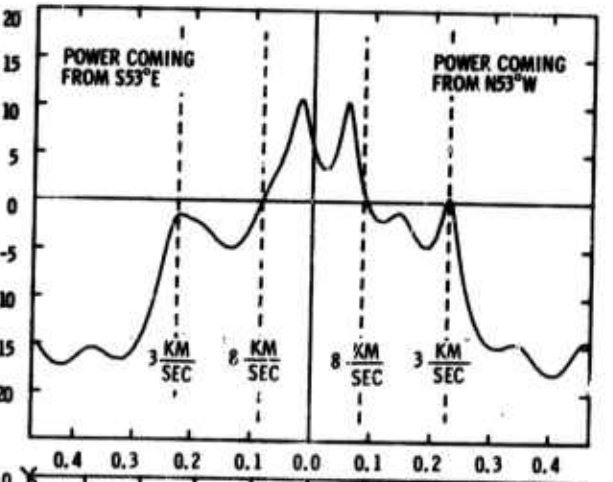


INTEGRATED FRACTIONAL POWER FROM THE S $37^{\circ}$ W - N $37^{\circ}$ E ARM VS VELOCITY IN KM/SEC



WAVENUMBER POWER SPECTRA FROM THE S $53^{\circ}$ E - N $53^{\circ}$ W ARM IN db VS CYCLES/KM

0.75280 CPS



INTEGRATED FRACTIONAL POWER FROM THE S $53^{\circ}$ E - N $53^{\circ}$ W ARM VS VELOCITY IN KM/SEC

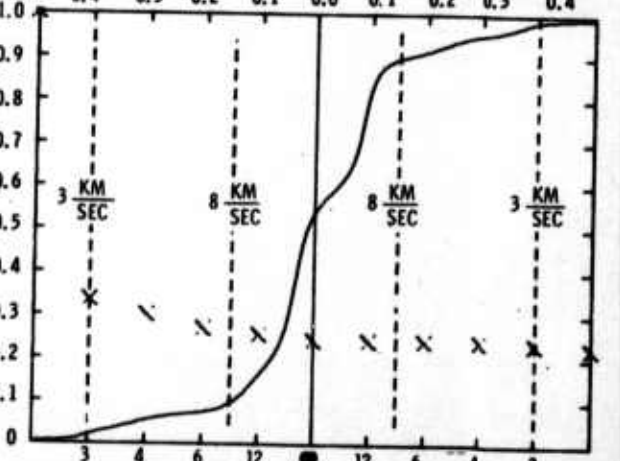
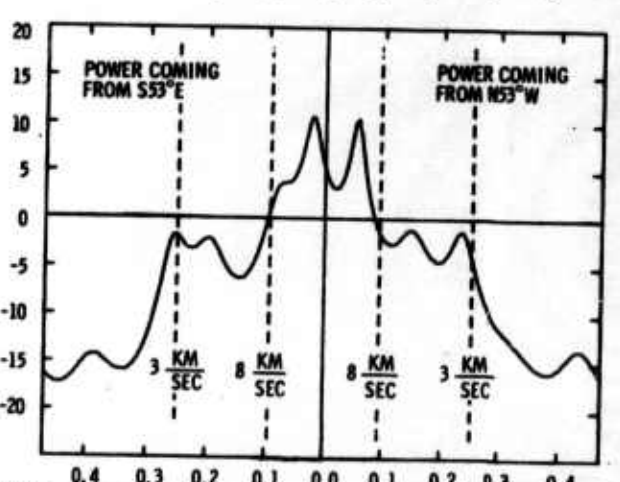
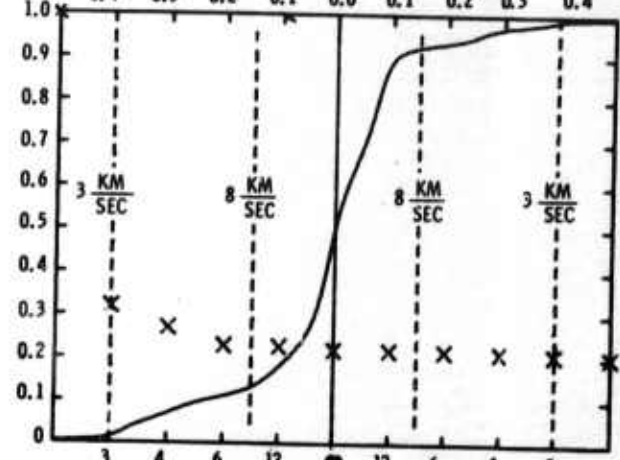
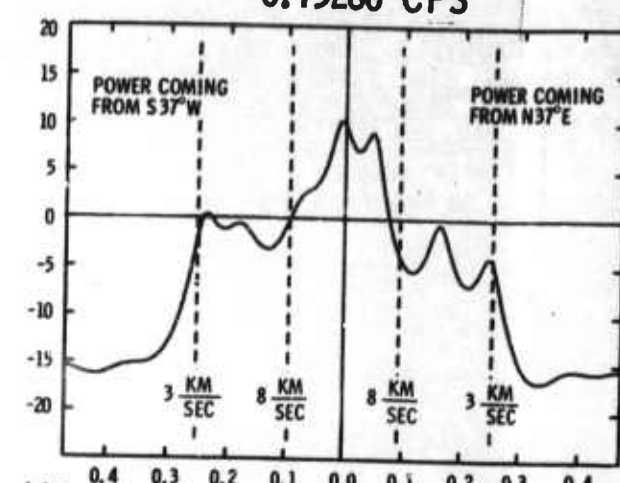
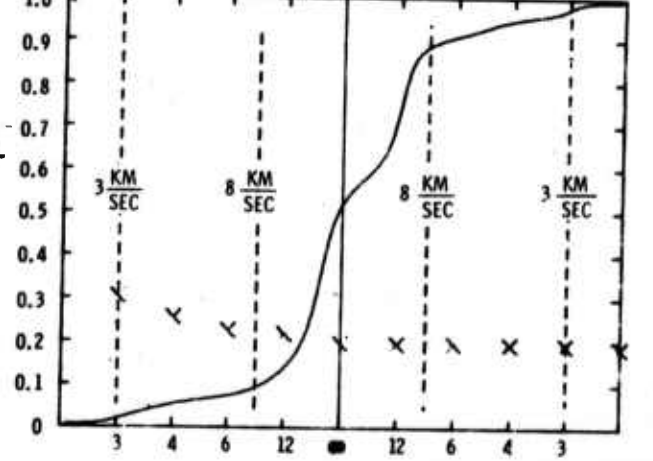
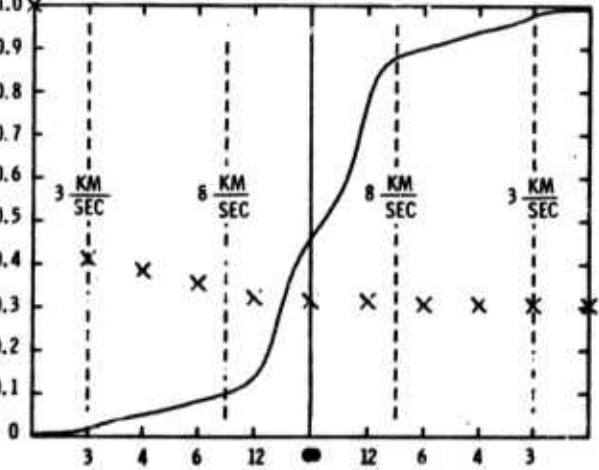
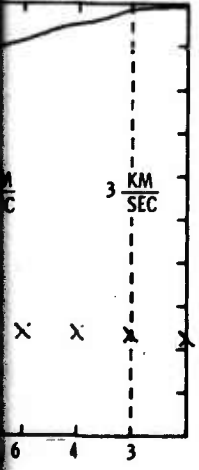
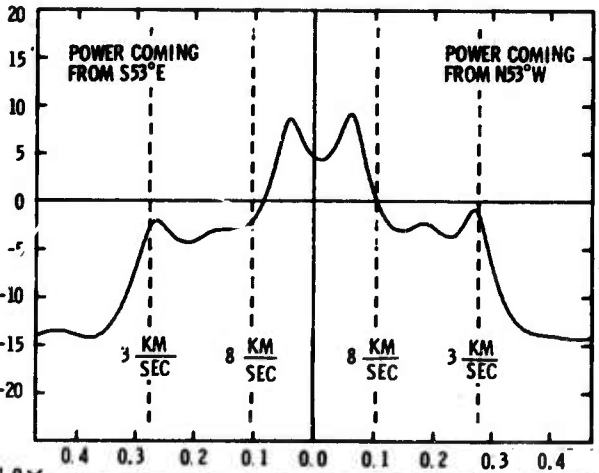
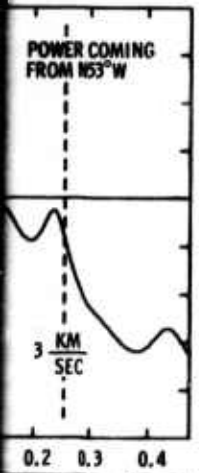
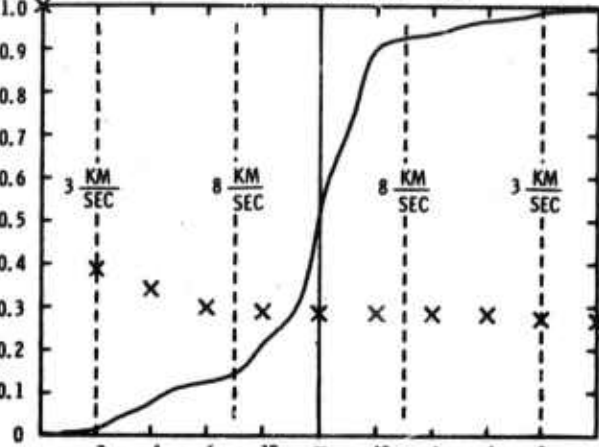
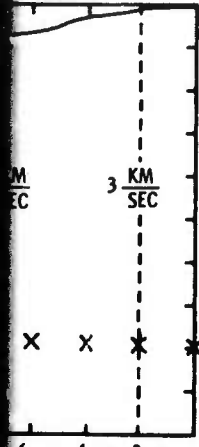
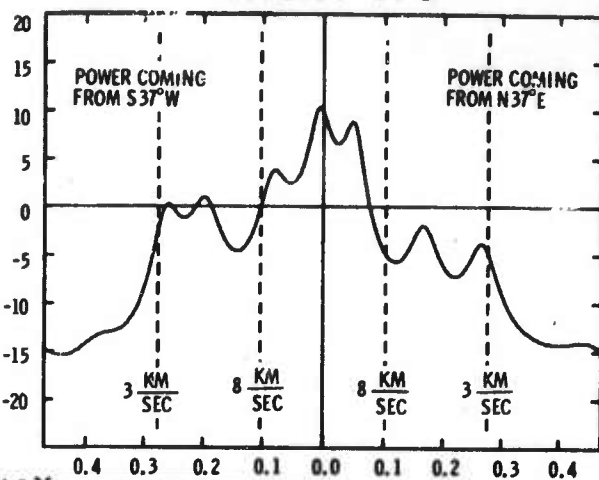
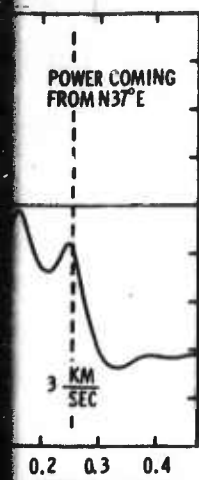


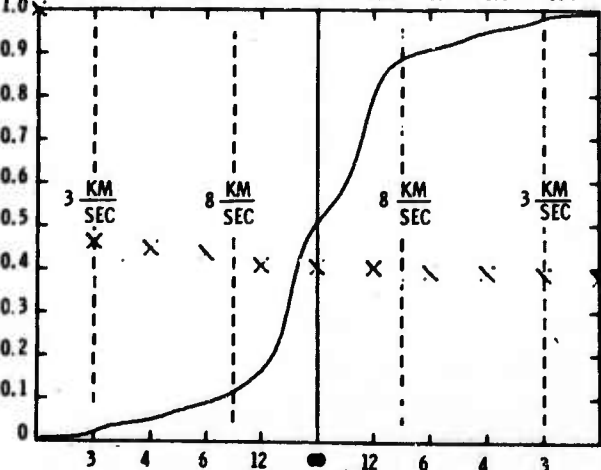
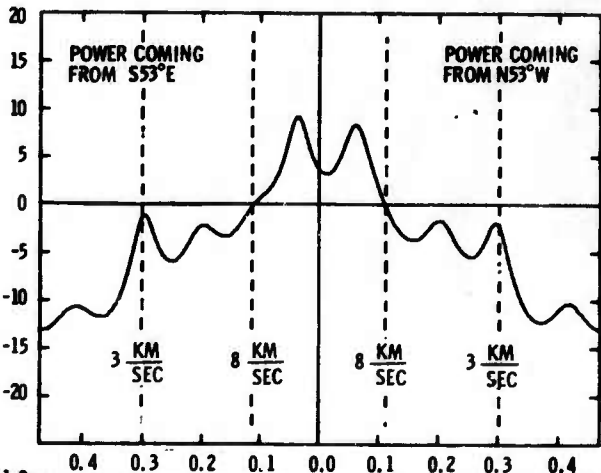
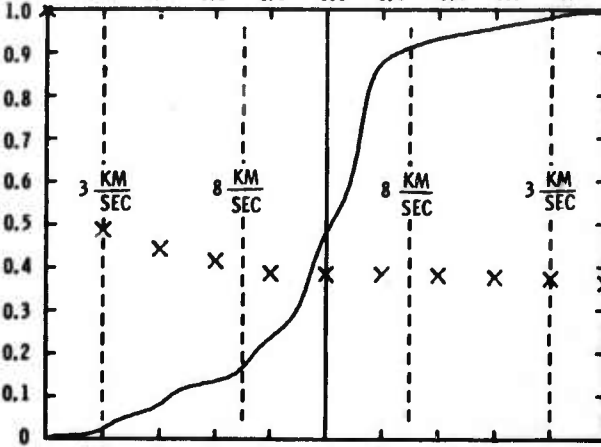
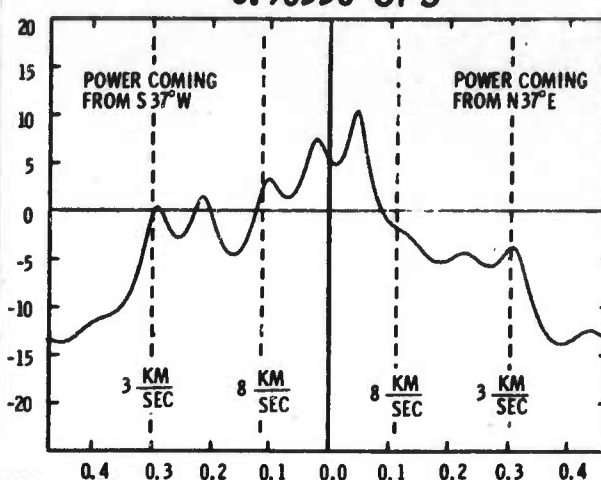
Figure 9. Wavenumber and Integrated Spectra From the Two TFO Arms at Frequencies

S

0.82808 CPS



0.90336 CPS



s at Frequencies of 0.67752, 0.75280, 0.82808, and 0.90336 cps

Z 13/14

WAVENUMBER POWER SPECTRA FROM THE S $37^{\circ}$ W - N $37^{\circ}$ E ARM IN db VS CYCLES/KM

INTEGRATED FRACTIONAL POWER FROM THE S $37^{\circ}$ W - N $37^{\circ}$ E ARM VS VELOCITY IN KM/SEC

WAVENUMBER POWER SPECTRA FROM THE S $53^{\circ}$ E - N $53^{\circ}$ W ARM IN db VS CYCLES/KM

INTEGRATED FRACTIONAL POWER FROM THE S $53^{\circ}$ E - N $53^{\circ}$ W ARM VS VELOCITY IN KM/SEC

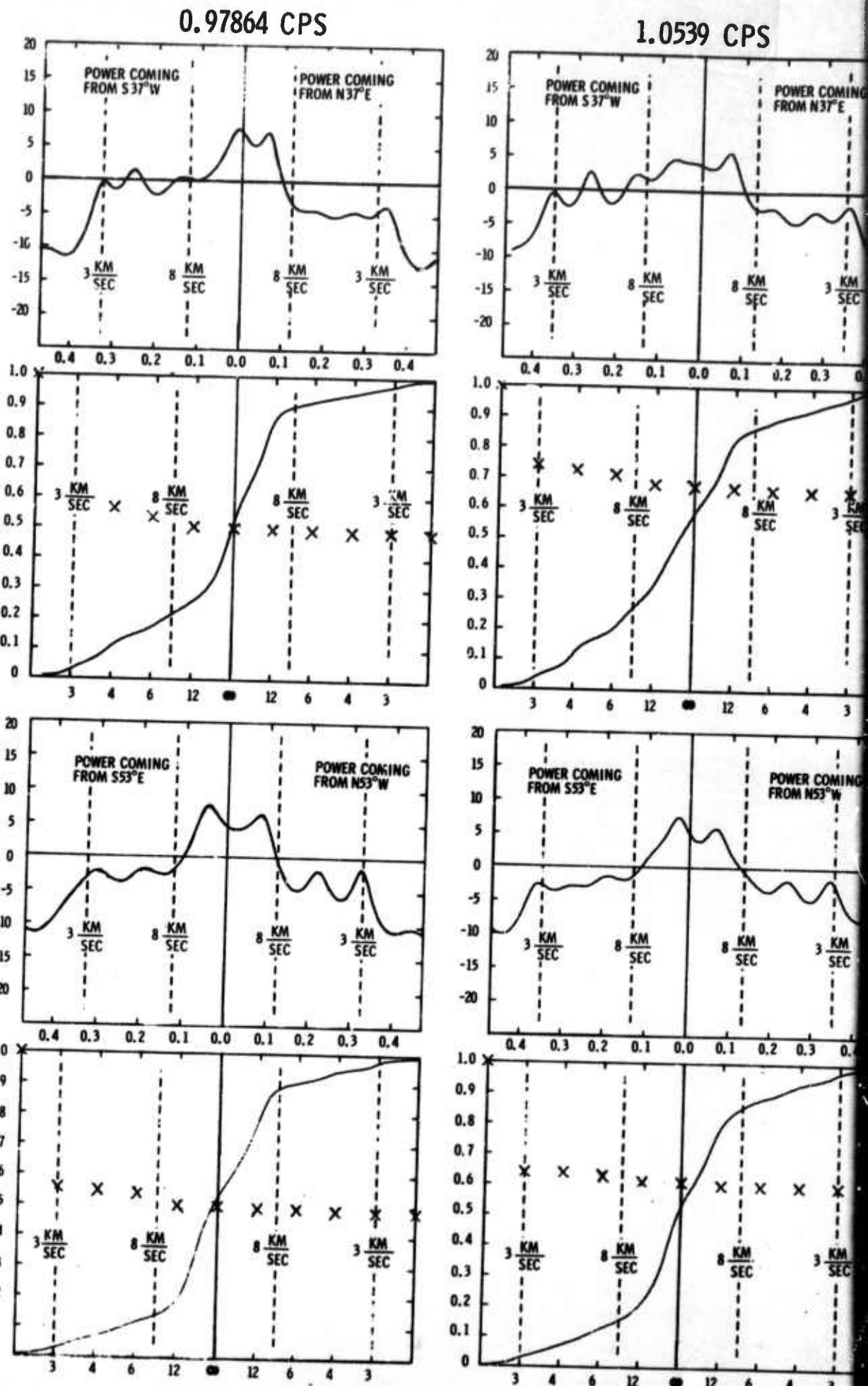
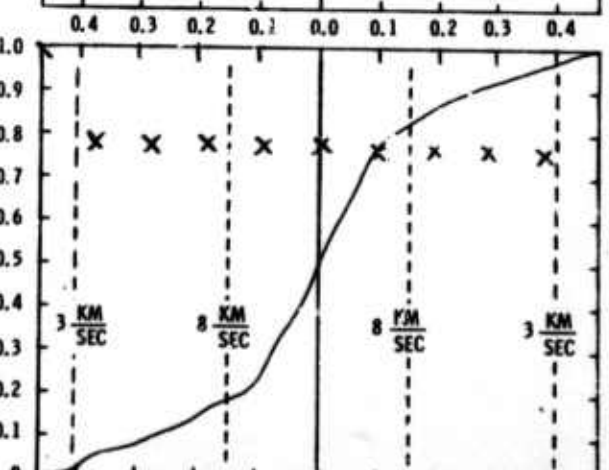
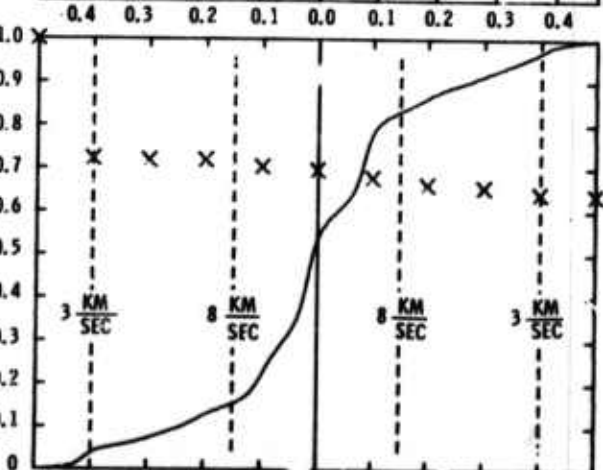
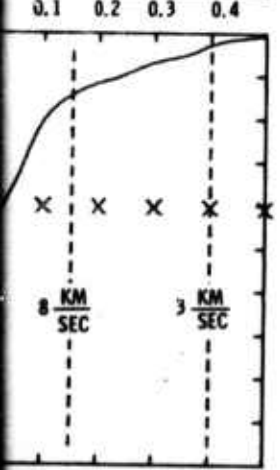
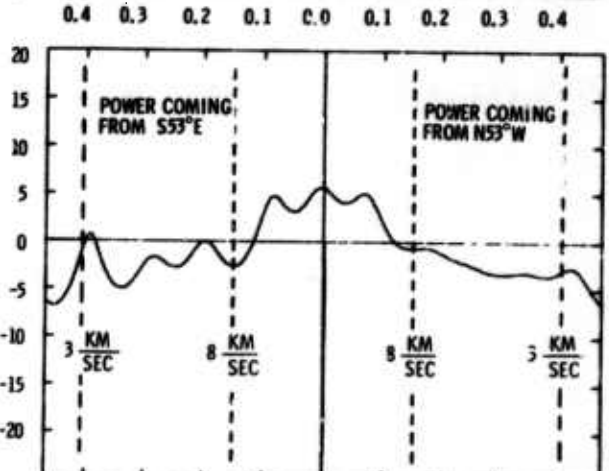
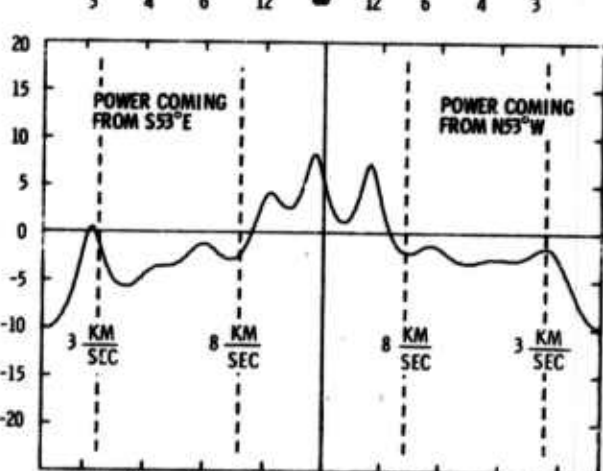
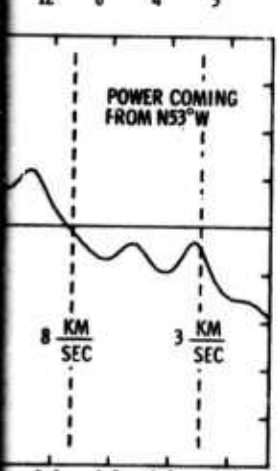
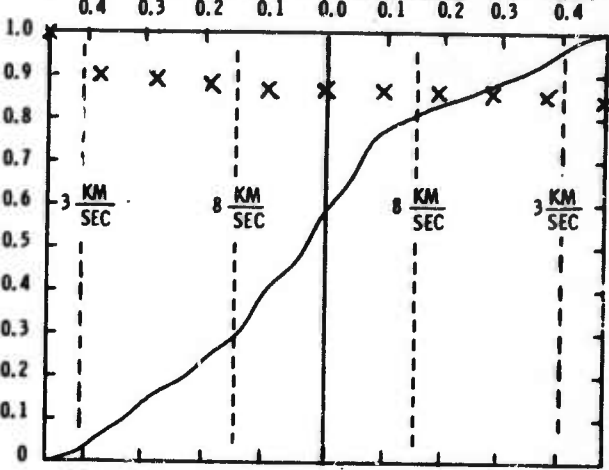
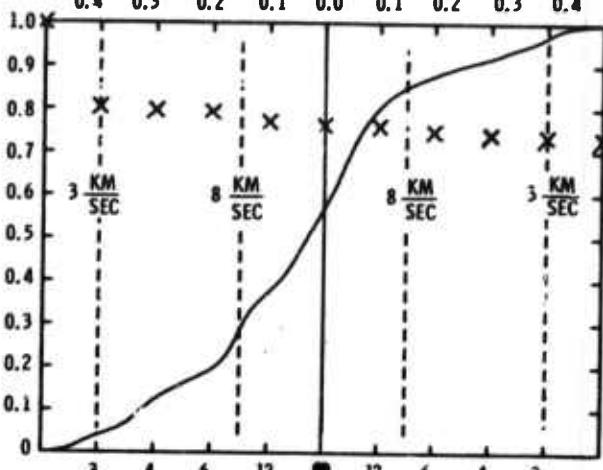
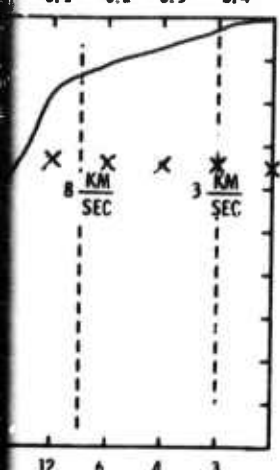
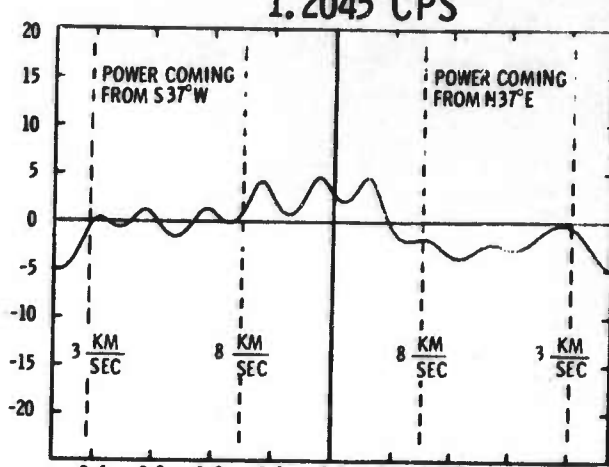
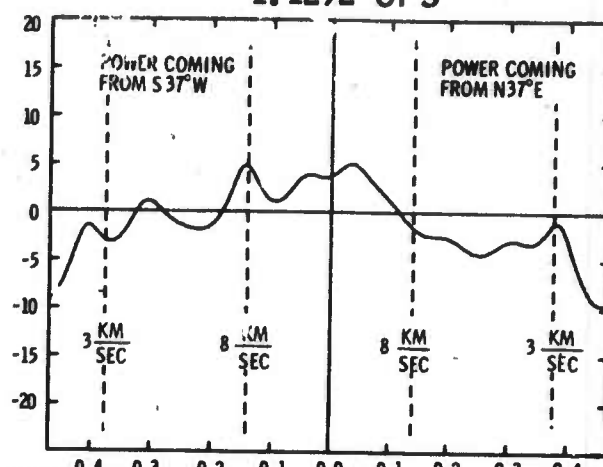
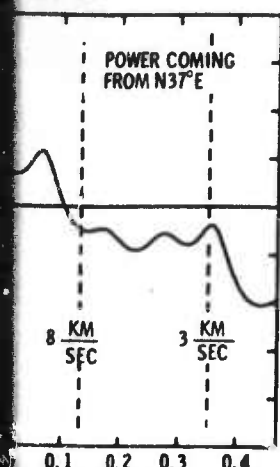


Figure 10. Wavenumber and Integrated Spectra From the Two TFO Arms at Frequencies 0.97864 CPS and 1.0539 CPS.

CPS

1.1292 CPS

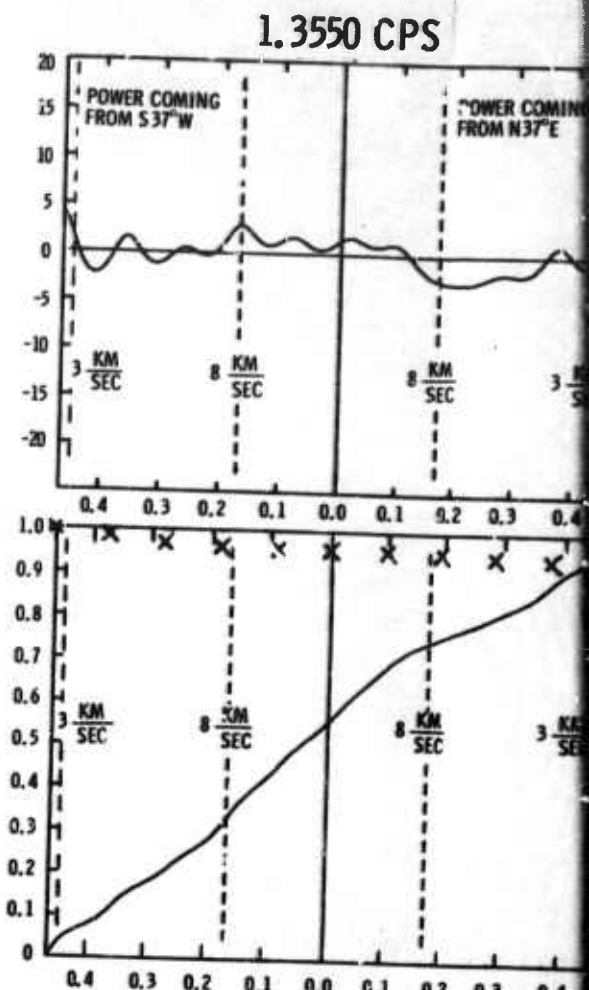
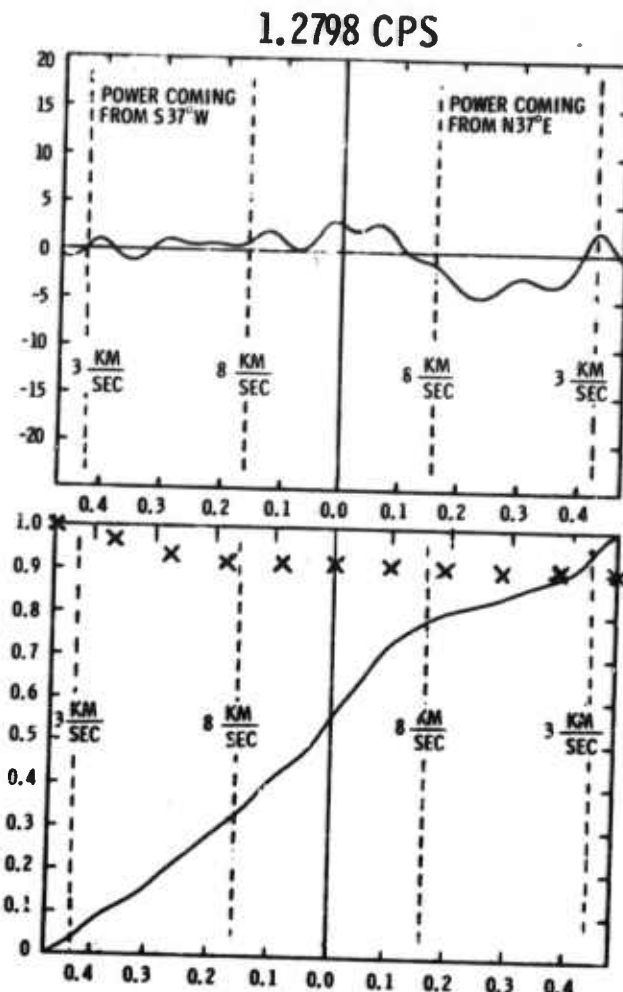
1.2045 CPS



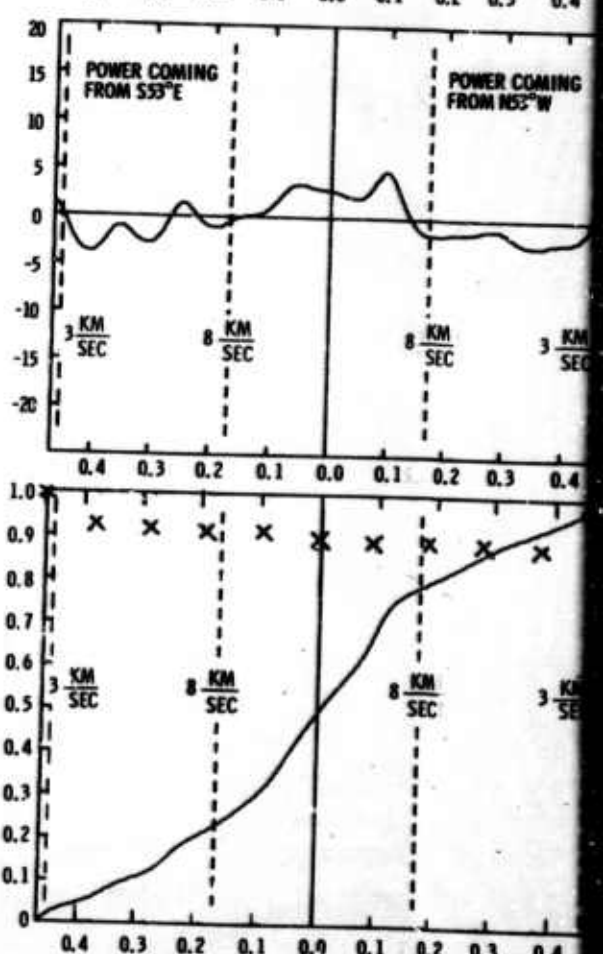
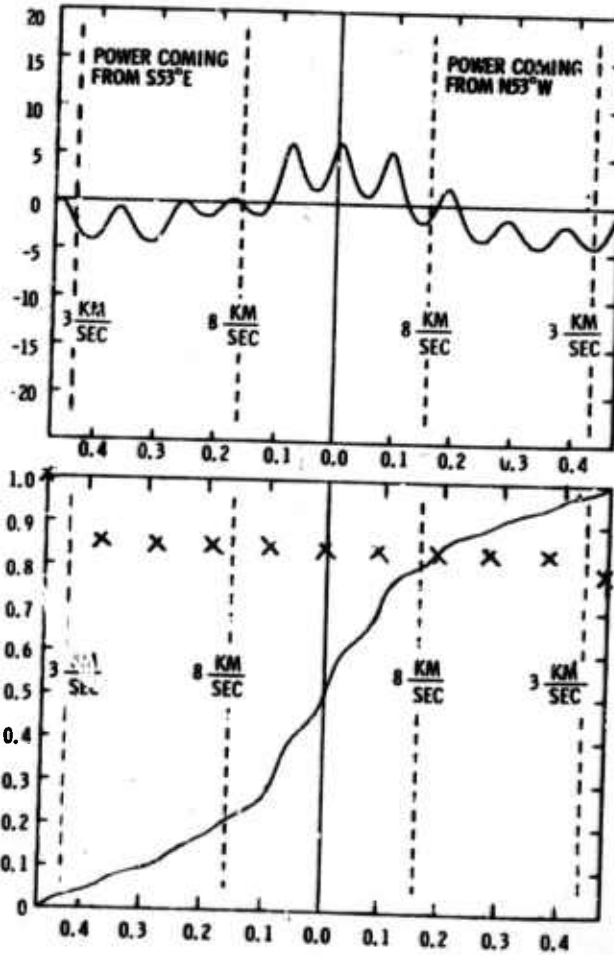
Arms at Frequencies of 0.97864, 1.0539, 1.1292, and 1.2045 cps

15/16

WAVENUMBER POWER SPECTRA FROM THE S $37^{\circ}$ W - N $37^{\circ}$ E ARM IN db VS CYCLES/KM



WAVENUMBER POWER SPECTRA FROM THE S $53^{\circ}$ E - N $53^{\circ}$ W ARM IN db VS CYCLES/KM



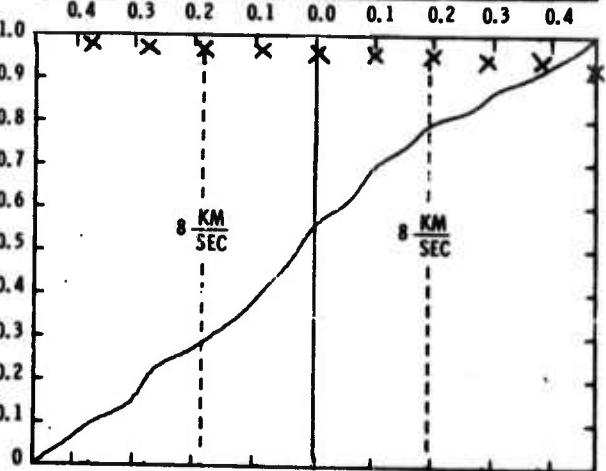
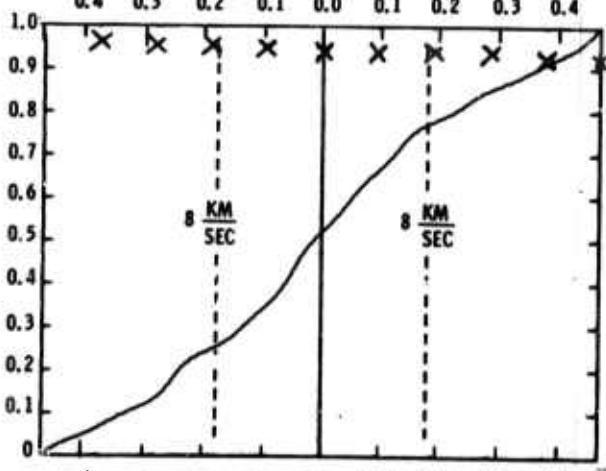
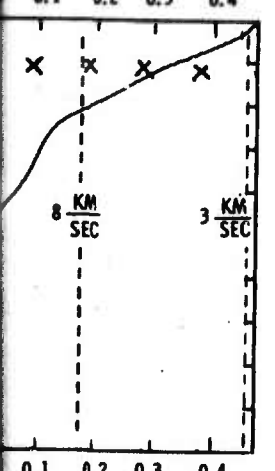
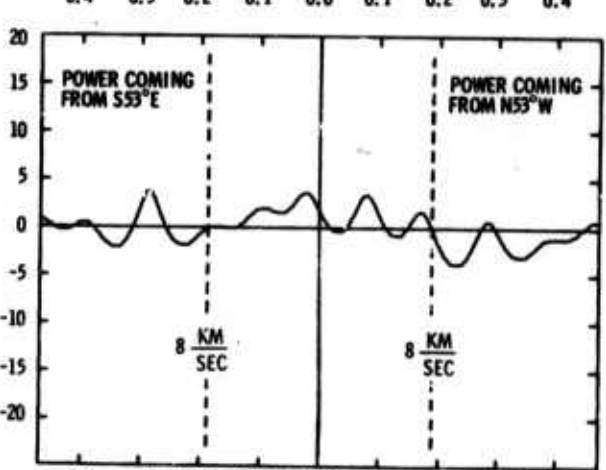
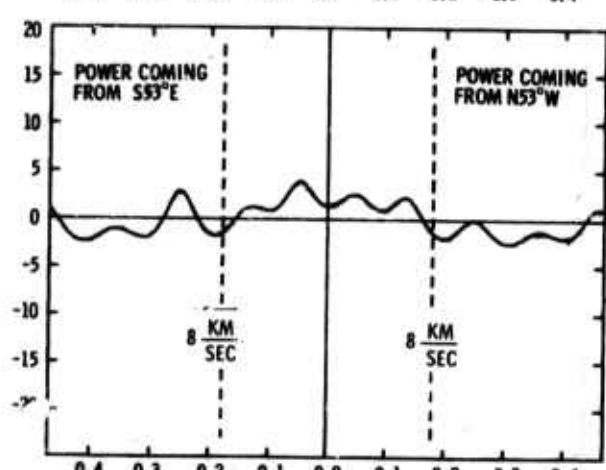
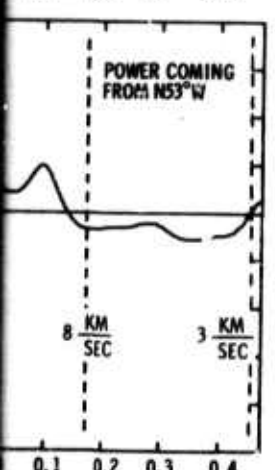
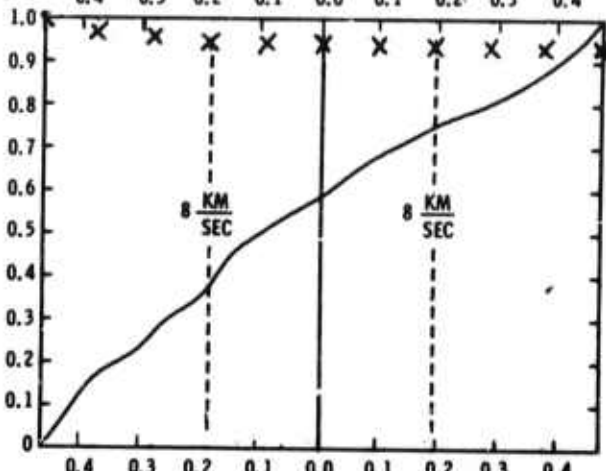
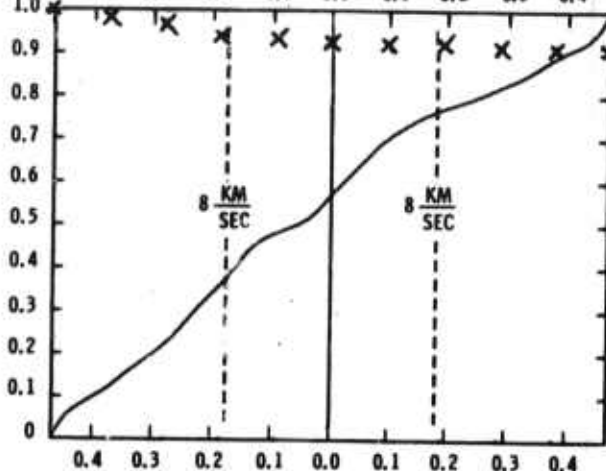
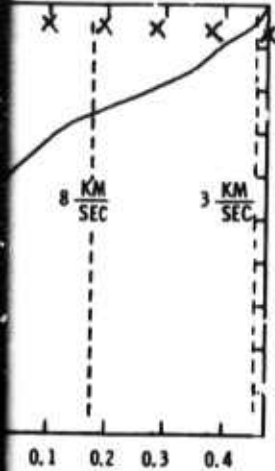
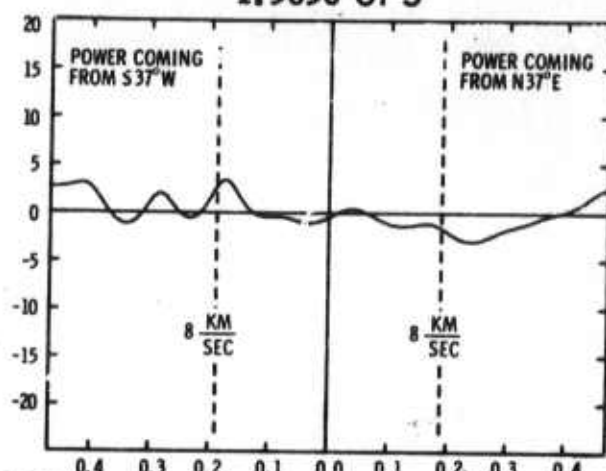
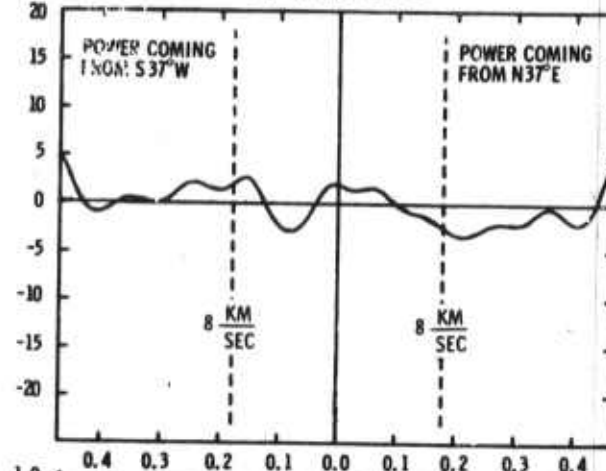
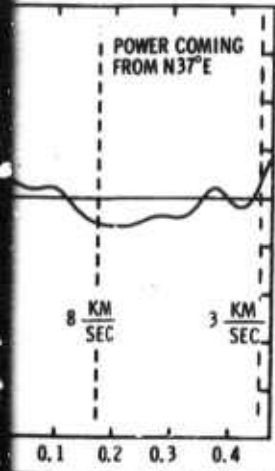
INTEGRATED FRACTIONAL POWER FROM THE S $53^{\circ}$ E - N $53^{\circ}$ W ARM VS WAVENUMBER IN CYCLES/KM

Figure 11. Wavenumber and Integrated Spectra From the Two TFO Arms at Frequencies 1.2798 CPS and 1.3550 CPS.

CPS

1.4303 CPS

1.5056 CPS

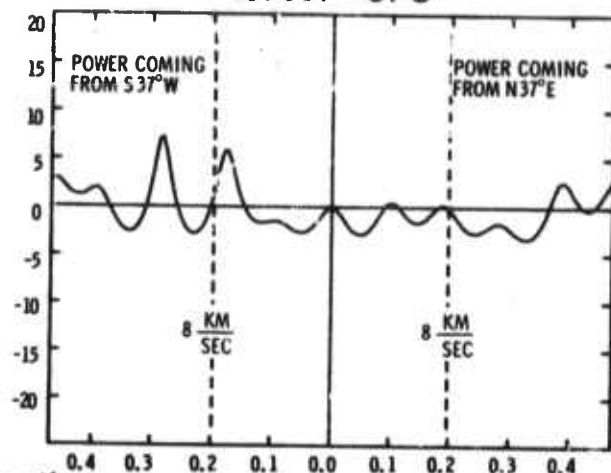


Arms at Frequencies of 1.2798, 1.3550, 1.4303, and 1.5056 cps

17/18

WAVENUMBER POWER SPECTRA FROM THE S37°W - N37°E ARM IN db VS CYCLES/KM

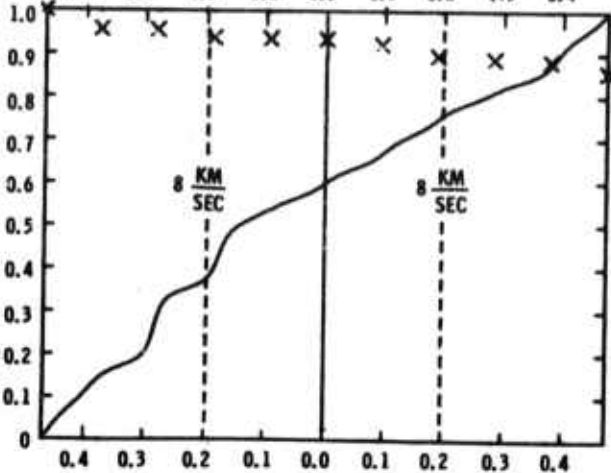
1.5809 CPS



INTEGRATED FRACTIONAL POWER FROM THE S37°W - N37°E ARM VS WAVENUMBER IN CYCLES/KM

WAVENUMBER POWER SPECTRA FROM THE S53°E - N53°W ARM IN db VS CYCLES/KM

1.6562 CPS



INTEGRATED FRACTIONAL POWER FROM THE S53°E - N53°W ARM VS WAVENUMBER IN CYCLES/KM

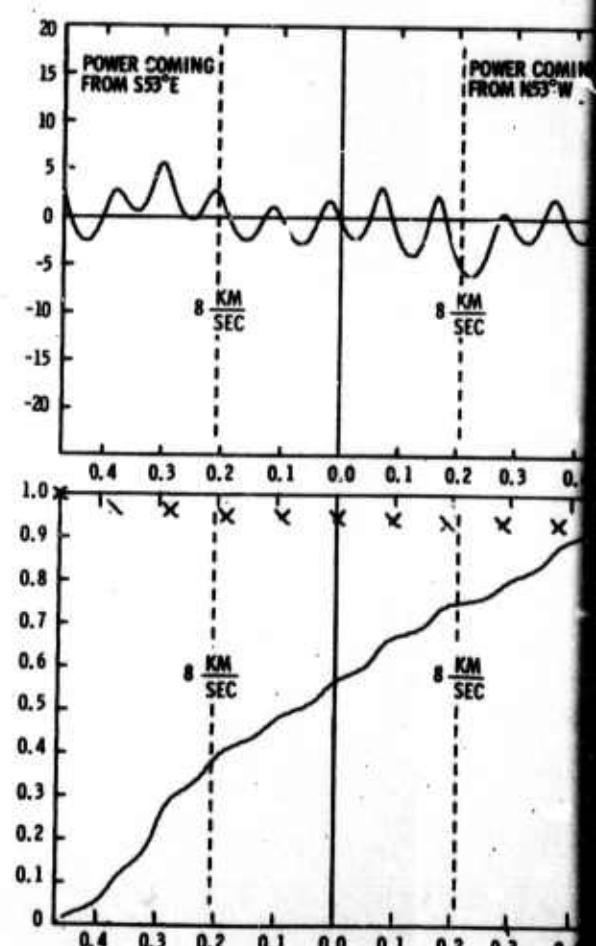
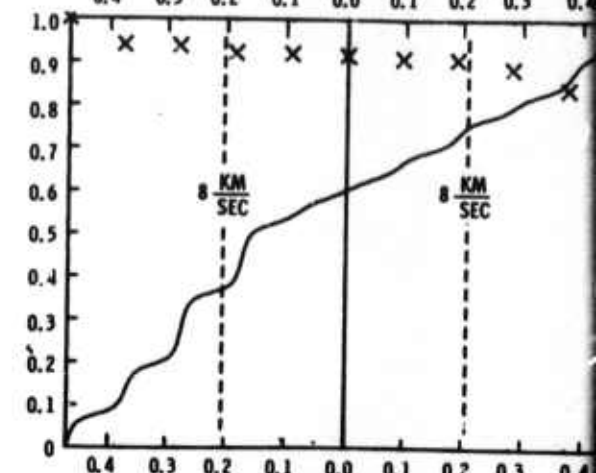
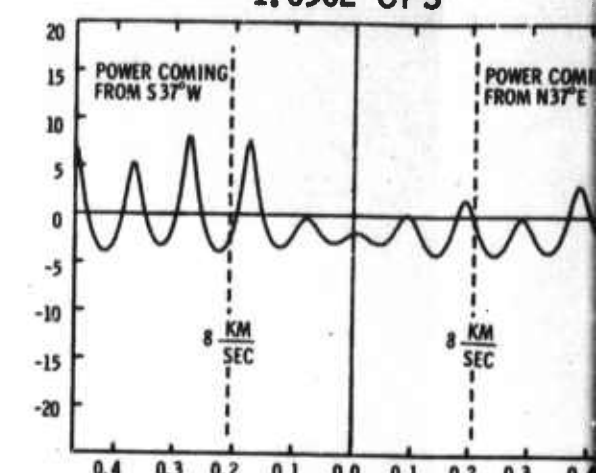
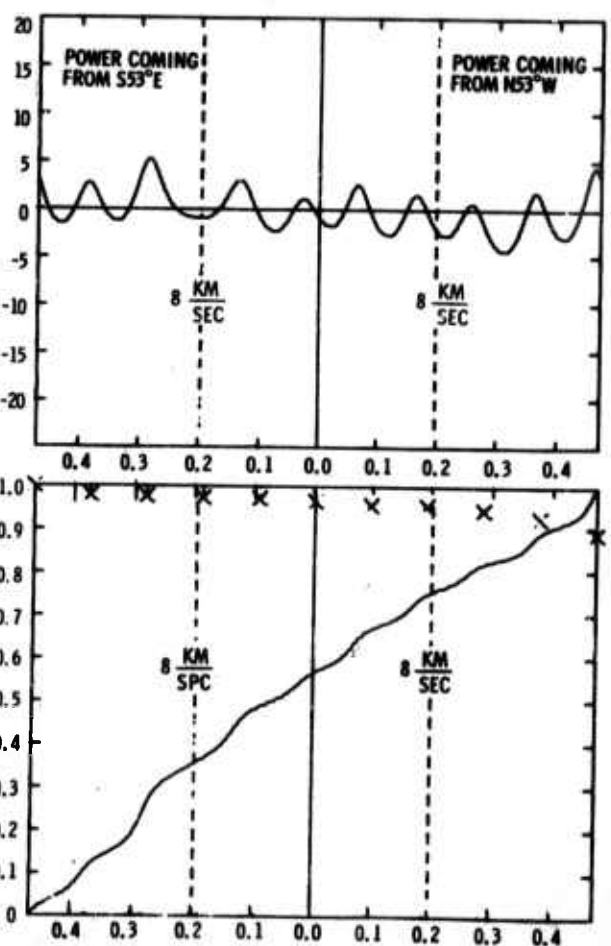
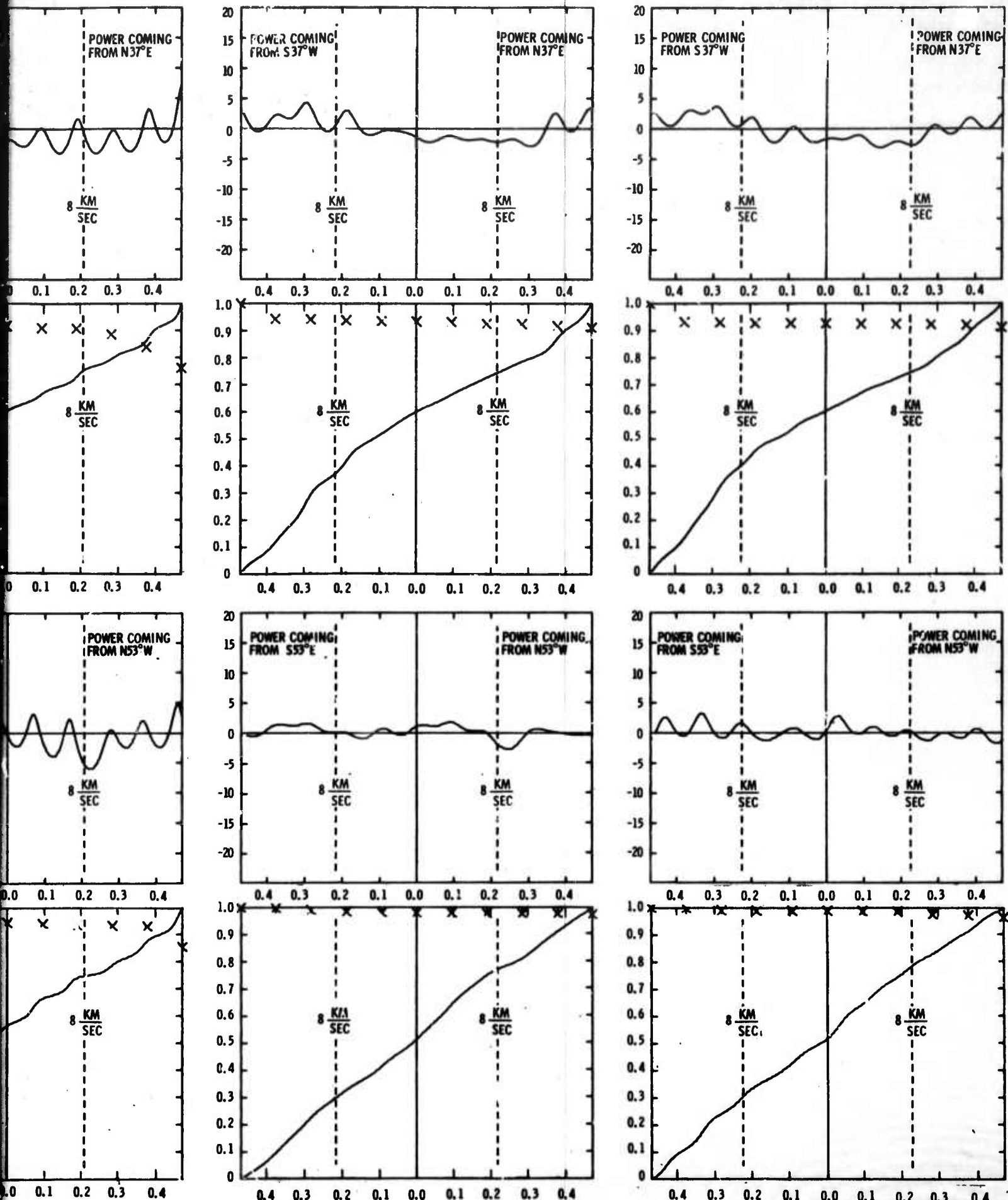


Figure 12. Wavenumber and Integrated Spectra From the Two TFO Arms at Frequencies 1.5809 and 1.6562 CPS.

CPS

1.7314 CPS

1.8067 CPS



Arms at Frequencies of 1.5869, 1.6562, 1.7314, and 1.8067 cps

19/20

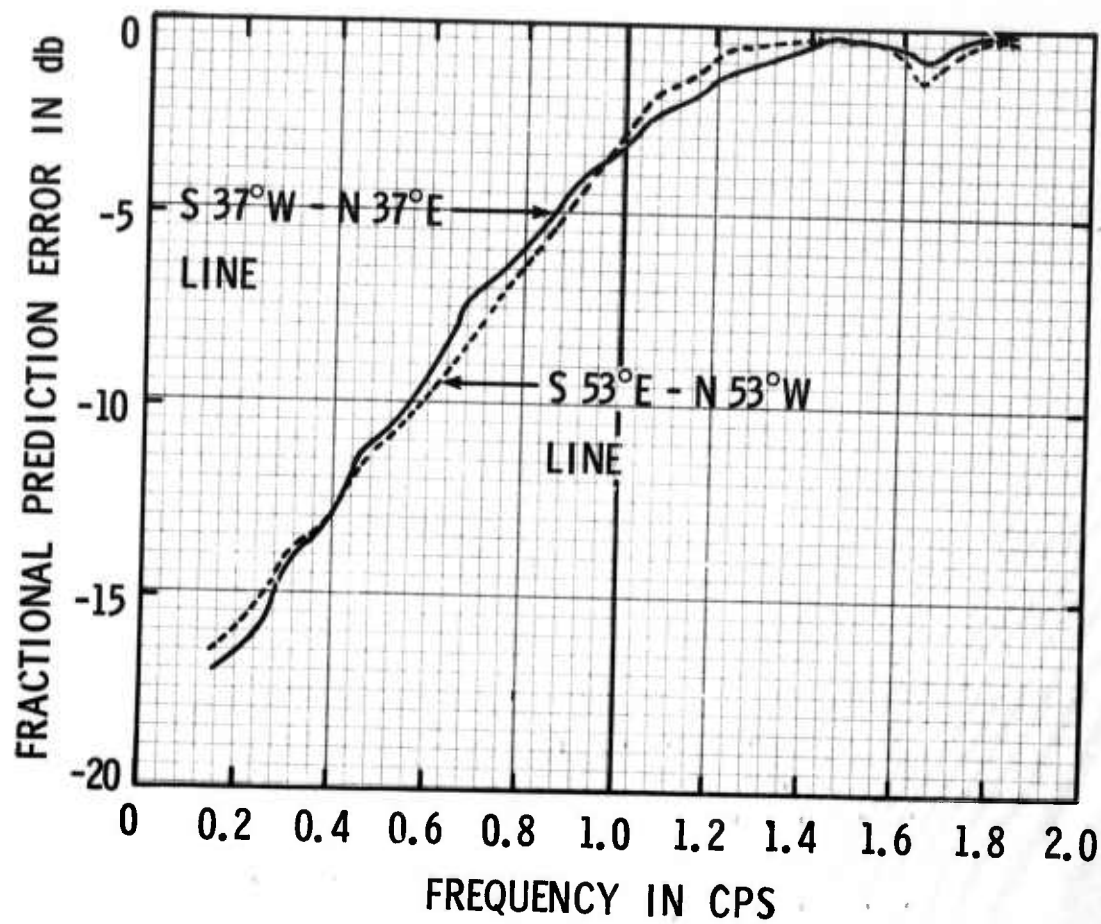


Figure 13. Fractional Prediction Error in db vs Frequency For Predicting One Seismometer Ahead Using a Line of Ten Seismometers



## SECTION IV

### GENERAL FEATURES OF THE K-LINE WAVENUMBER SPECTRA

In surveying the general properties of the wavenumber spectra presented in Figures 7 through 12, perhaps the most striking feature is the precipitous drop in the power density outside of the 3 km/sec dashed lines. This phenomena indicates the excellent quality of the ambient seismic noise recording and the high resolution of the data analysis, since any energy traveling at velocities lower than that of the fundamental Rayleigh wave (which is the slowest mode of seismic propagation) is not seismically interpretable.

A second striking feature is the predominance of power at P-wave velocities; i. e., power between the 8 km/sec lines, in the frequency range of 0.30112 cps to 1.2045 cps. This P-wave noise splits into two peaks at 0.37640 cps and becomes well separated at higher frequencies. These two peaks correspond to the two storms which have already been correlated with this noise sample.<sup>2</sup> The weather during the time of this noise sample is shown in Figure 14.

A third feature is the very strong, highly direction Rayleigh wave in the low frequency plots. This wave was generated by a storm hitting the coast of Newfoundland. The Rayleigh wave noise, which tends to be inline with the S37°W to N37°E arm, dies out quickly as the frequency increases. At 0.52696 cps and above more low velocity power is coming from the S37°W direction than from the N37°E direction. This higher frequency Rayleigh wave noise apparently is caused by the nearby Pacific Ocean which appears to be rather calm as indicated by the weather map in Figure 14. At frequencies above 1.2045 cps, the Rayleigh wave noise

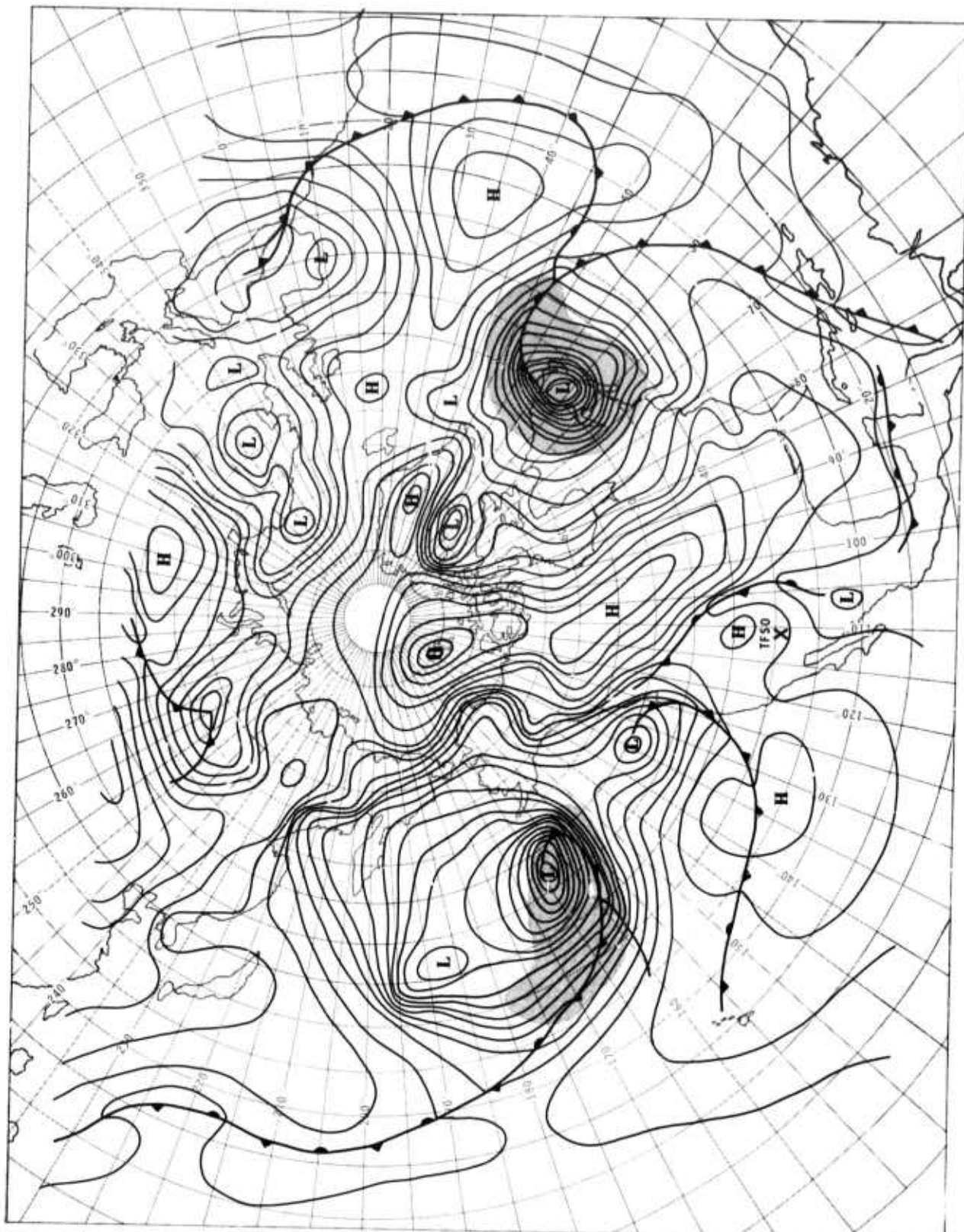


Figure 14. Surface Weather Map at 0600 GMT (12-20-63)



has filled the wavenumber unit cell from -0.47 to +0.47 cycles/km, and the mantle P-wave energy is disappearing. This whitish spectrum results in low seismometer-to-seismometer predictability, as is indicated by the x's in the integrated power density plots. The anomalous peaks in the wavenumber spectra near 1.6 cps are the only details of interest at these higher frequencies. This anomaly and a similar one near 2.0 cps, both caused by lines in the frequency spectrum of this noise (Figure 4), could not be interpreted.

Figure 15 shows the estimated absolute frequency power spectra of the various noise components previously discussed. These power spectra, shown as recorded by the JM-PTA system, can be changed to ground motion spectra by using the response curve of Figure 3. More detailed discussions of the various noise components and how their absolute spectra were estimated are given in the next few pages of this report.

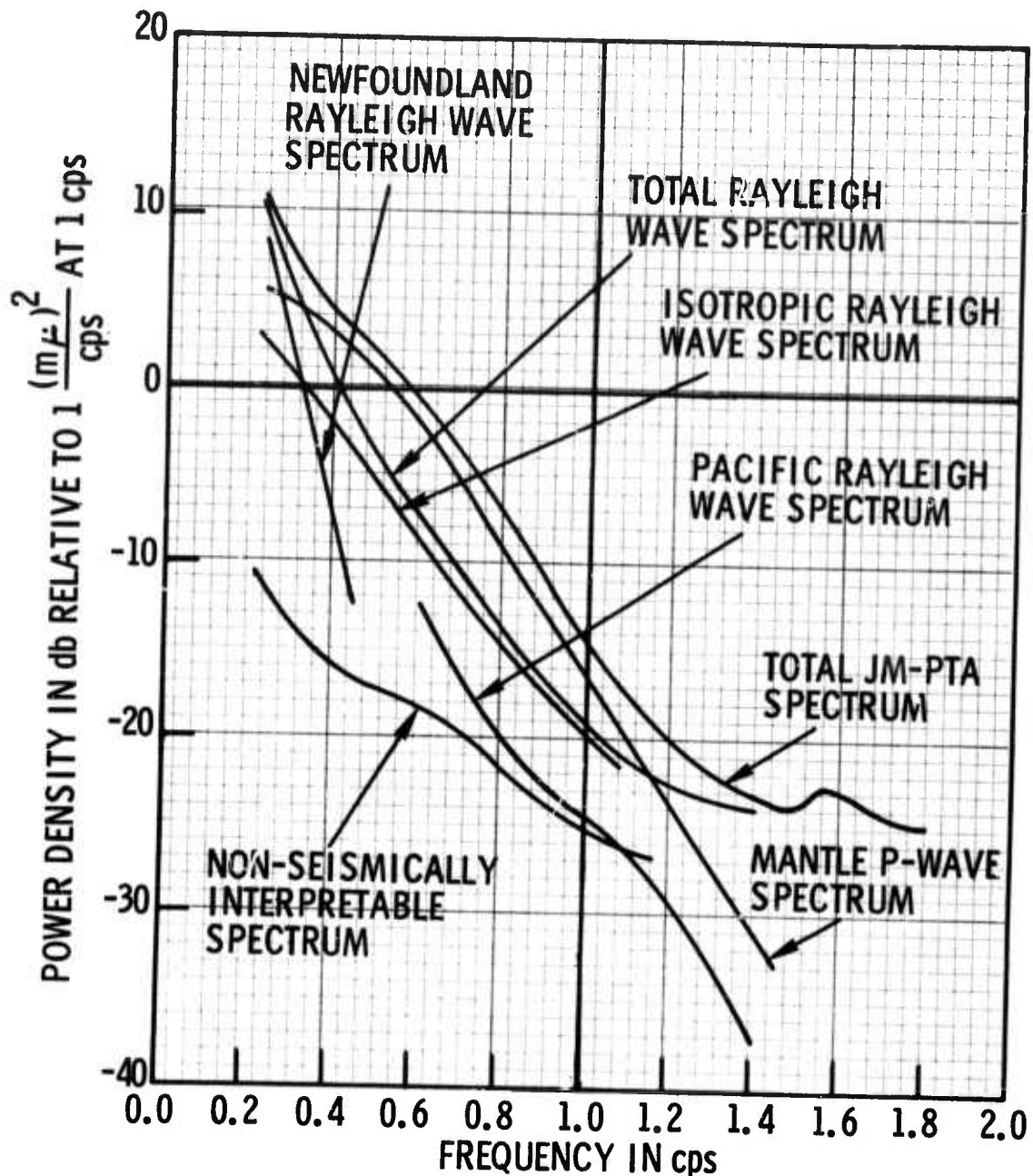


Figure 15. Absolute Frequency Power Spectra in db vs cps For Various Noise Components in the TFO Long Noise Sample



---

## SECTION V

### THE NONSEISMICALLY INTERPRETABLE NOISE

Noise appearing at velocities lower than the velocity of the fundamental Rayleigh wave cannot be interpreted as plane wave, space-stationary, seismically propagating energy because the slowest seismic propagation mode at the TFO array, which is built on bare granite or on thin overlying sediments, is the Rayleigh wave.

This nonseismically interpretable noise is undoubtedly a sum of several types of noise. Three possibly important sources are seismometer system noise, locally generated noise such as wind noise, and acoustic or air-ground coupled noise. However, these three noise sources are probably minor, especially above 1 cps, compared to the leakage of true seismic noise energy into nonseismic velocity regions. This leakage is caused by real-earth deviations from the assumed uniform space-sampling of a homogeneous, space stationary earth. This assumption is the basis of wavenumber analysis. Local and widespread nonuniformity of the earth, e.g., elevation differences of several hundred feet common at TFO, and the fact that distances between the seismometers in a line vary considerably, causes confusion in the wavenumber analysis of the data. As the seismic wavelength decreases (and the frequency increases), the effects of the nonuniformity of the earth becomes more pronounced, causing this type of leakage to become more severe.

Figure 15 shows absolute frequency spectrum of the nonseismically interpretable noise in the frequency range from 0.22584 cps to 1.2045 cps. The spectrum was obtained by estimating the db level of the wavenumber spectra outside of the seismic band of wavenumbers and



---

then combining this estimate with the absolute frequency spectrum estimate of the total recorded noise. Absolute frequency spectrum estimates for this type of noise were not made below 0.22584 cps because of the difficulty in making accurate low frequency measurements with short period instrumentation. Estimation of the spectrum above 1.2045 cps was impossible because the Rayleigh wave energy filled up the unit cell.



---

## SECTION VI

### MANTLE P-WAVE NOISE

Bodywave noise or mantle P-wave noise is operationally defined in this report to mean seismic energy with horizontal velocity higher than 8 km/sec. This type of noise shows up first in the wavenumber spectra at 0.22584 cps, increases in percentage until at 0.60224 cps it is about 80 percent of the total noise and then decreases until beyond 1.4 cps it can no longer be accurately estimated. The absolute frequency spectrum of this high velocity noise is shown in Figure 15. This spectrum was estimated mainly from the wavenumber spectra of the S37°W to N37°E line of the array since the directional Rayleigh wave energy was clearly separated along this arm. The fact that broadside Rayleigh wave energy also contributes to the amount of apparent high velocity energy has been considered in making these estimates.

Starting at 0.37640 cps and continuing somewhat beyond 1 cps, the mantle P-wave energy is separated into two peaks. These peaks, noted in Special Report No. 17<sup>2</sup> although not as clearly, were associated with two storms (Figure 14). Figure 16 shows the velocities estimated from the seven frequency plots (0.52696 to 0.97864 cps, labeled 1 through 7) of the noise coming from these two storms. These independent velocity estimates were obtained from the wavenumber values of the two pairs of mantle P-wave peaks appearing along the two lines of the array, with the correct pairing of the peaks being decided from the 2-dimensional spectra shown in Special Report No. 17.<sup>2</sup> Except for the 0.52696 cps estimate of the Pacific storm peak, these two 7-point sets have surprisingly little scatter. However, this small scatter is greatly magnified when these velocities are transformed onto their corresponding surface source



locations through use of the P-wave propagation paths through the body of the earth. These corresponding surface source positions, also labeled 1 through 7, are superimposed on the weather map shown in Figure 17. The Pacific storm is reasonably well covered by these points; however, the points for the storm off the coast of Newfoundland seem to be too far south. Considering the small size of the array at TFO, the accuracy of these estimates is surprisingly good. In any case, there can be little doubt that these storms do produce these two mantle P-wave peaks and that they are the major source of the bodywave energy in the TFO long noise sample.

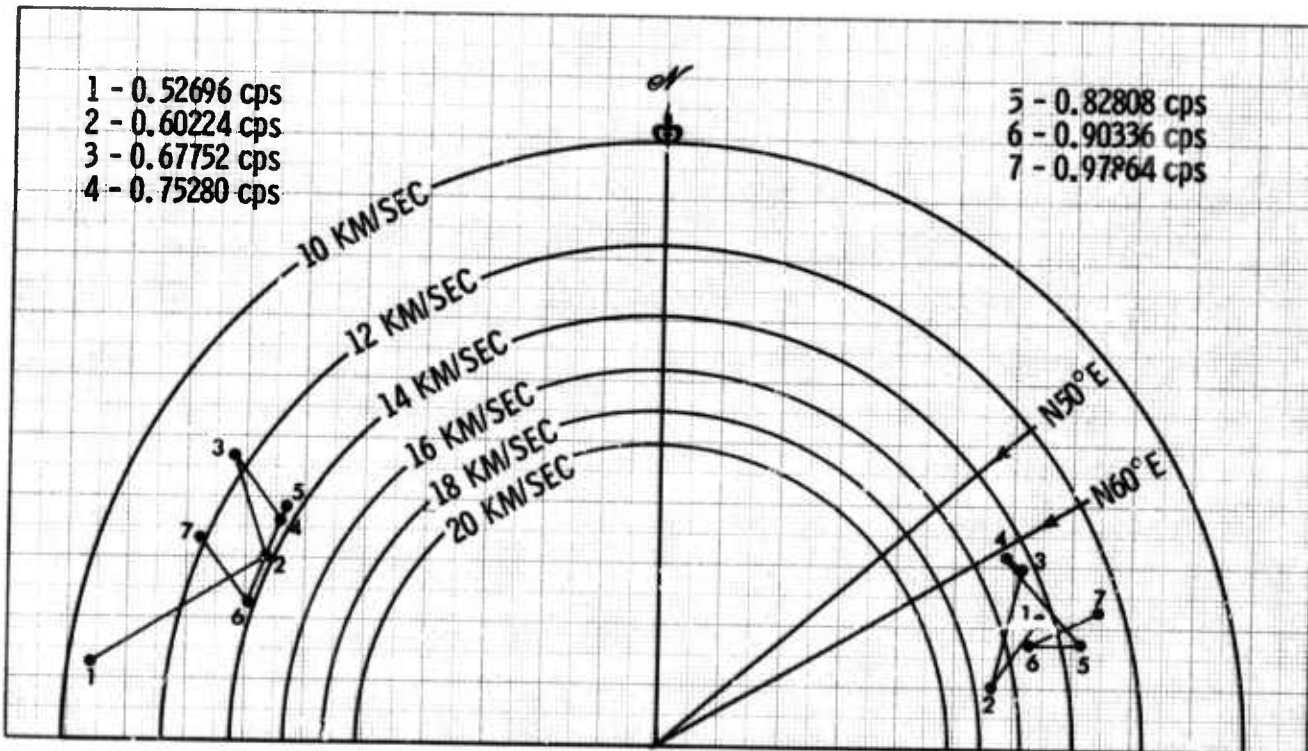


Figure 16. Estimated Vector Velocities of the Two Mantle P-Wave Peaks as a Function of Frequency

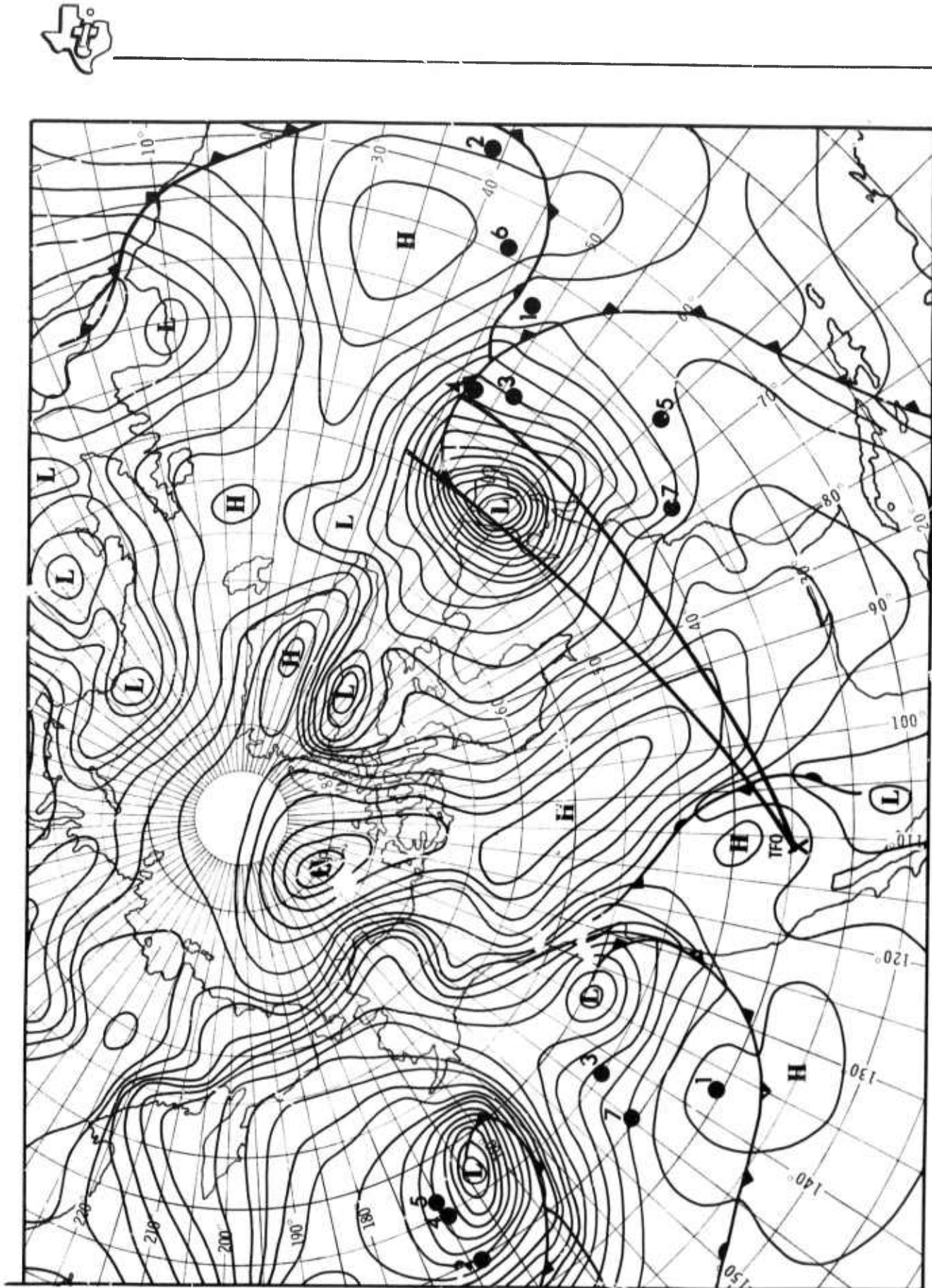


Figure 17. Estimated Surface Locations of the Mantle P-Wave Energy



## SECTION VII

### RAYLEIGH WAVE NOISE

It has been known for a long time that the TFO long noise sample contains a very strong and highly directional 6-sec Rayleigh wave coming from the northeast. The simplest proof of this energy is found in low-pass filtered playbacks of the original data (Figure V-24 in Special Report No. 2<sup>3</sup>). In Figure 7, this Rayleigh wave shows up on the S37°W to N37°E plots as a sharp peak near the right-hand 3 km/sec dashed line and on the S53°E to N53°W plots as a peak just to the left of the center line. The plot at 0.07528 cps in Figure 7 is actually of little significance since it is simply a lower resolution picture of the plot at 0.15056 cps. This leakage of power is easily understood by looking at Figure 4 and noting that, in these high resolution power spectra, the power density at 0.07528 cps is at least 20 db down from that at 0.15056 cps.

In estimating the velocity of this highly directional Rayleigh wave, it is immediately evident that the 0.15056 cps plot will give a velocity of about 3 km/sec, whereas the 0.22584 cps peak is at an appreciably higher velocity. This discrepancy is resolved by assuming that the main Rayleigh wave power lies at intermediate frequencies. To further investigate this, wavenumber spectra for the two arms were calculated at 0.18820 cps and are shown in Figure 18. Starting with the 0.15056 cps plot, the velocity estimates f/k were 3.06, 3.52 and 3.85 km/sec for an average of 3.48 km/sec. The direction of the Rayleigh was consistently estimated as coming from N50°E. These values are perhaps more accurate than the values of 3.4 km/sec and N60°E estimated in Semiannual Technical Report No. 3.<sup>1</sup> These estimates are probably about as accurate as can be measured with a 10-km dia array at these low frequencies. Great circle arcs passing through TFO at N50°E and N60°E are shown in Figure 17.

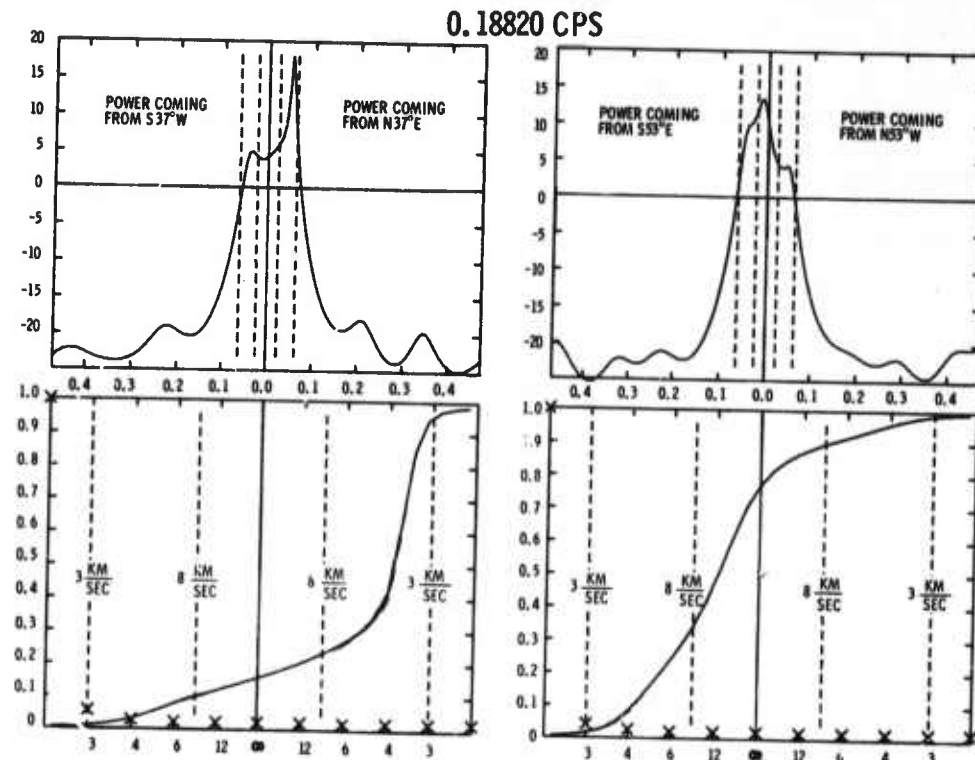


Figure 18. Wavenumber and Integrated Spectra From the Two TFO Arms at the Frequency of 0.18820 cps

The principal result obtained from these wavenumber spectra is the clear proof of nondirectional energy traveling at the Rayleigh wave velocity. This is the first time that this postulated energy has been seen directly. Its presence had been noted from its effect on multichannel filters designed from noise samples, but this energy had not been seen on previous wavenumber spectra; e.g., see Figures 2 through 7 of Special Report No. 17.<sup>2</sup>

The Rayleigh wave energy was estimated as being the residual energy after the P-wave and nonseismically interpretable noise was subtracted from the total energy. The absolute frequency spectrum of the total Rayleigh wave energy is shown in Figure 15. This total Rayleigh wave



---

energy was separated into three components:

- Energy coming from the direction of Newfoundland
- Energy coming from the general direction of the Pacific Ocean
- Nondirectional or isotropic Rayleigh-wave energy

This separation is based on the imbalance in the wavenumber spectra along the S37°W to N37°E line of the array. For low frequencies up to 0.45 cps, there is more Rayleigh wave energy coming from the N37°E direction, i. e., from the direction of the storm which is hitting the coast of Newfoundland at the time of the noise sample. The absolute frequency spectrum of this extra N37°E energy is shown in Figure 15 and labeled as the Newfoundland Rayleigh wave. At higher frequencies, the imbalance reverses and more energy comes from the S37°W direction, i. e., from the general direction of the Pacific Ocean. The absolute frequency spectrum of this extra S37°W energy is shown in Figure 15 and labeled as the Pacific Rayleigh wave. It should be noted that these interpretations are consistent with the observation that the wavenumber spectra along the S53°E to N53°W line are nearly balanced in Rayleigh wave energy. The residual, nondirectional Rayleigh wave energy has its absolute frequency spectrum labeled as isotropic Rayleigh wave energy in Figure 15.

The rapid decay with frequency of the Newfoundland Rayleigh wave energy (about 170 db/cps for the ground motion spectrum) undoubtedly reflects the frequency dependent absorption of inelastic attenuation. The Pacific Rayleigh wave energy decays much less rapidly with frequency (about 45 db/cps for the ground motion spectrum). This gentler slope of the spectrum is consistent with the fact that the Pacific Ocean is much closer to TFO than is the coast of Newfoundland. The lack of simultaneous spectra from other locations vitiates any further analysis of this phenomena.

In Figures 7 through 10, where the Rayleigh wave energy is still contained in the wavenumber unit cell, it can be seen that the cutoff velocity for seismic noise seems to decrease as the frequency increases.



In fact, this is an experimental observation of Rayleigh wave dispersion. Figure 19 shows the cutoff velocity measurements of the seismic noise as a function of frequency. Although these measurements have considerable scatter, the smooth curve appears to be a quite good estimate of the Rayleigh wave dispersion at TFO.

In the 1.2798 cps wavenumber plot (Figure 11), the Rayleigh wave energy has just finished filling the wavenumber unit cell (-0.47 to +0.47 cycles/km). Continuing on into the next three higher frequency plots, the folding back of this energy begins to double (3-db higher) the spectra at the edges of the unit cell. This phenomena indicates that these spectra are seismically valid and that if the unit cell were larger, i. e., if the seismometer spacing were smaller, then the dropoff into a nonseismic region would still occur. This observation should be carefully considered by anyone designing the geometry of a new seismic array at TFO.

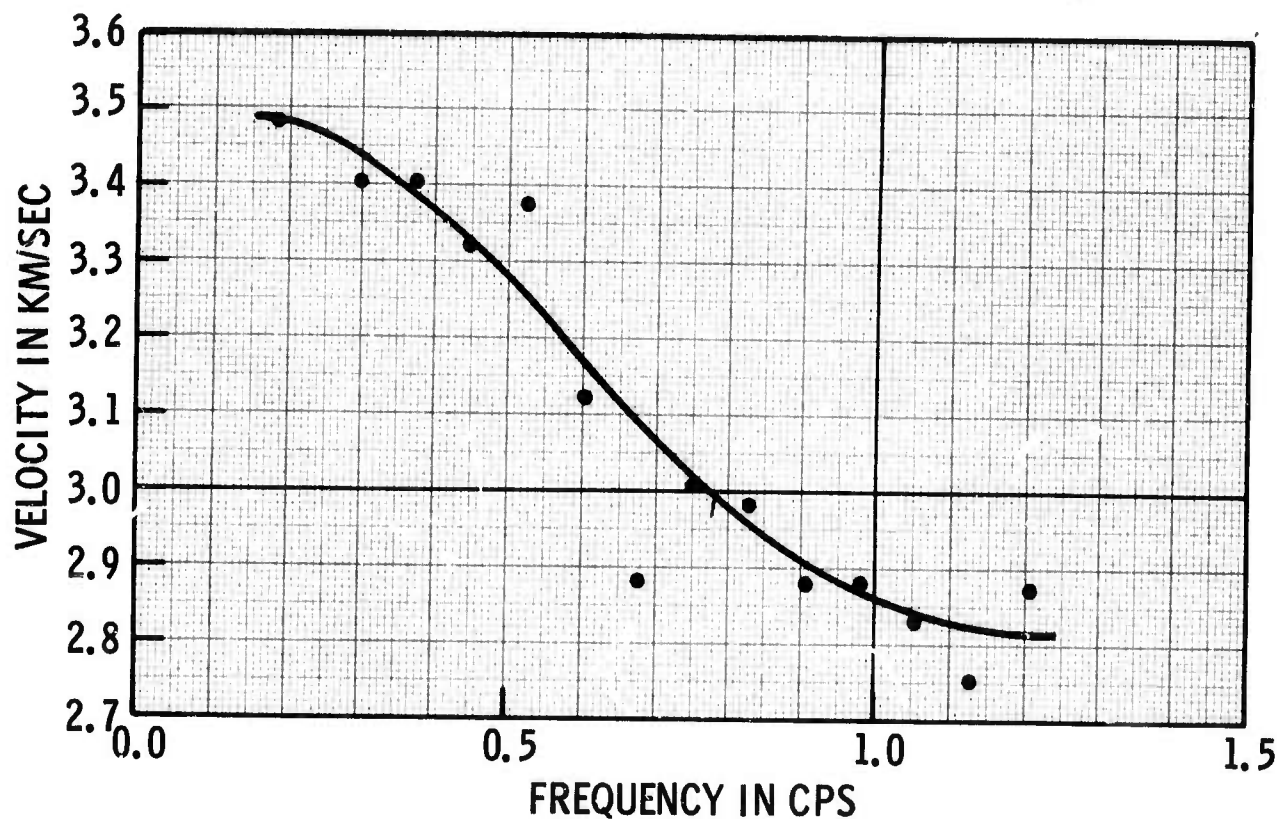


Figure 19. Estimated Velocity of the Rayleigh Wave at TFO as a Function of Frequency



---

## SECTION VIII

### LINE SPECTRA

From the frequency power spectra shown in Figure 4 and from the work given in Array Research Semiannual Technical Report No. 3,<sup>1</sup> it is evident that the TFO long noise sample contains two pure frequency lines below 2.3 cps. These two frequencies, one at 1.61 cps and the other at 2.06 cps, exhibit strong coherence between many pairs of seismometers (Figures V-11, V-12, VI-19, VI-20, VI-21, VI-22, and VI-23 in Array Research Semiannual Technical Report No. 3<sup>1</sup>), but they do not appear to possess space-stationary correlation functions (Figures VI-6, VI-11, and VI-16 in Semiannual Technical Report No. 3). Even though these line spectra make up a large percentage of the high frequency seismic power, their source and propagation characteristics remain a mystery. These spectra are documented here for future reference.

The effect of the 1.61 cps line on the wavenumber spectra can be seen in Figure 12 in the 1.5809 cps and 1.6562 cps plots. The "ringingness" of these spectra is quite different from the white spectra at higher and lower frequencies. To examine this phenomena more closely, three wavenumber spectra were obtained at 1.6185 cps and are shown in the top portion of Figure 20. The left-hand plot is for the S37°W to N37°E arm and the right-hand plot is for the S53°E to N53°W arm. Both spectra are obtained in the same manner as that used for Figures 7 through 12. The center plot is a slightly lower resolution version of the right-hand spectrum. This middle spectrum was obtained because the sharp drop in the eleventh point prediction error made the right-hand plot of questionable validity. The lower three wavenumber spectra in Figure 20 are the same as the top three except that the frequency is 2.0702 cps which is very near the 2.06 cps line.

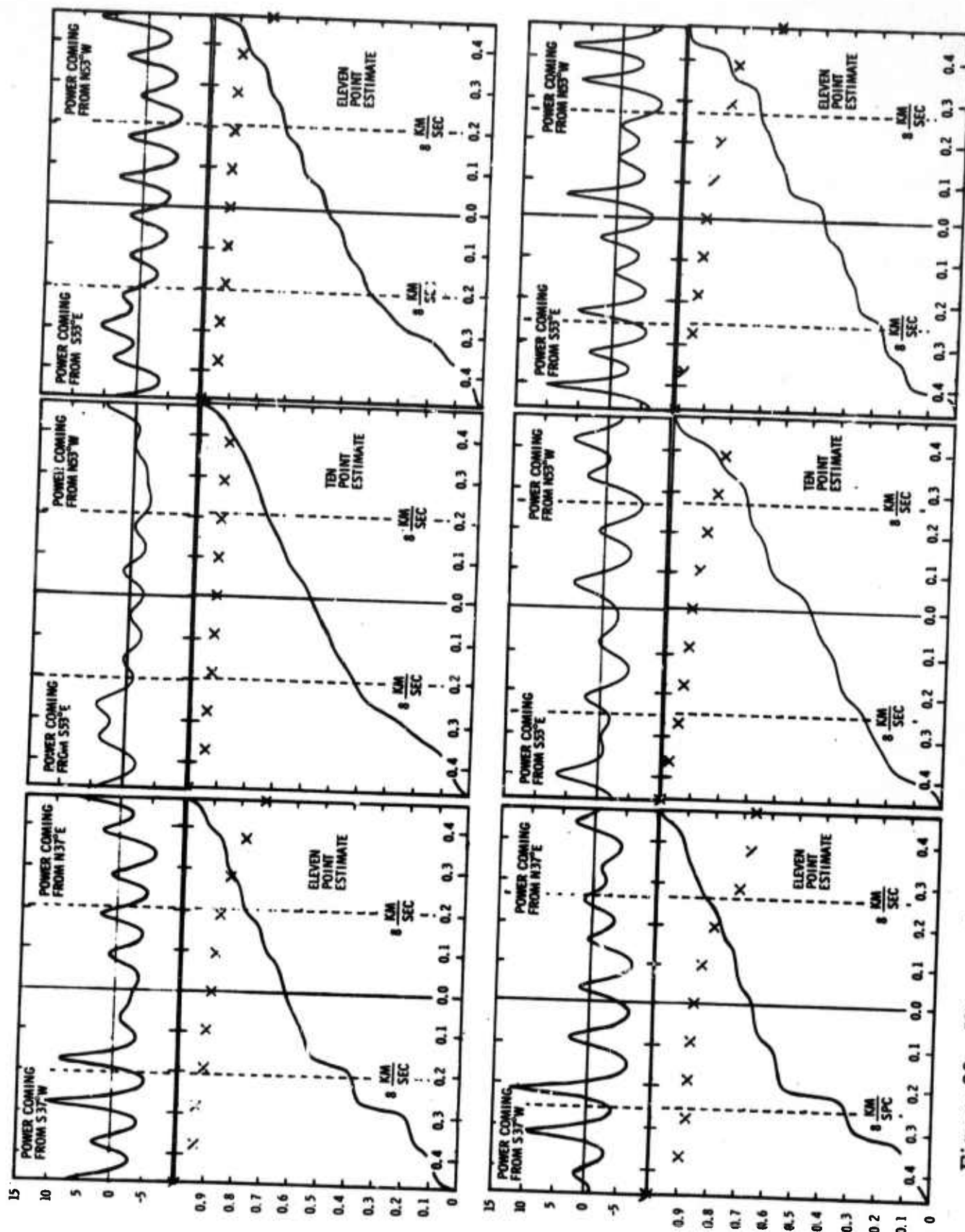


Figure 20. Wavenumber and Integrated Spectra From the Two TFO Arms at the Frequencies of 1.6185 cps (above) and 2.0702 cps (below)



---

The two spectra for the S37°W to N37°E arm are of interest in that a similar pair of peaks straddle the left-hand plots at 8 km/sec velocity. This observation indicates that these two frequency lines might have the same spatial origins. However, the four spectra for the S53°E to N53°W arm seem to be uninterpretable. Perhaps someday, when more is known about these pure frequency lines, these spectra will be understood.



---

## SECTION IX

### PROPERTIES OF THE NEW WAVENUMBER SPECTRAL ESTIMATION TECHNIQUE

In this section, the results of three studies into the properties of the new K-line wavenumber spectral estimation technique are presented. These studies are to acquire an understanding of the power and limitations of the new technique and to answer some hypothetical practical questions.

The first investigation made was to see how the new method compares with previous methods of wavenumber spectral estimation. Figure 21 shows the wavenumber spectra obtained in various ways from the power spectrum matrices for the S $37^{\circ}$ W to N $37^{\circ}$ E arm of the array at the frequencies of 0.15056, 0.37640, 0.75280, and 1.12920 cps.

The older methods, labeled Box Car, Half-Bartlett, Bartlett, and Hanning, first obtain an estimate of the space correlation function by averaging the crosspower spectra in the normalized power spectrum matrix that have the same space lags. The four correlation function estimates, one for each of the four frequencies, go from a space lag of -10 to +10 seismometer spacings and are complex conjugate symmetric about the zero lag value (which is unity due to the use of normalized spectrum matrices). The Box Car wavenumber estimate was obtained by directly Fourier transforming the correlation function estimates without applying any window weighting function. The Bartlett and Hanning estimates used these two well-known weighting functions on the correlations before Fourier transforming. The Half-Bartlett window, which is more or less defined here, is an average of the Box Car and the Bartlett windows with the triangular weighting coming down only halfway for the tenth lag values. Since the Box Car, the Half-Bartlett and the Hanning wavenumber spectral



---

estimates have negative power regions in some cases, the db plots were calculated using the logarithm of the absolute power spectrum. However, the Bartlett and the new method are mathematically prevented from having negative spectra. In comparing these techniques, Figure 21 shows the improved resolution and seismic credibility of the new method over the older methods of wavenumber spectral estimation.

The second study of this new technique examines how well the technique can estimate known theoretical wavenumber spectra. Figures 22 through 27 give the results of approximating six different wavenumber spectra (shown in the background of the plots), where the number of seismometers used varies from two to eleven. In particular, the top lefthand spectra show the approximation obtained with only two seismometers in the line. The bottom righthand spectra show the results obtained with 11 seismometers, the spacing between seismometers being held constant for all spectra.

The theoretical wavenumber spectra used in Figures 22 through 27 were generated from the familiar fixed speed, isotropic model for isotropic Rayleigh wave simulation and from the solid disk model for mantle P-wave representation. In Figures 22 and 23, the fixed speed isotropic model is used. This spectrum, when projected onto a line, has the mathematical form

$$P(k) = \frac{1}{\pi \sqrt{M^2 - k^2}} \quad \text{for } |k| \leq M$$

and

$$P(k) = 0 \quad \text{for } |k| > M$$

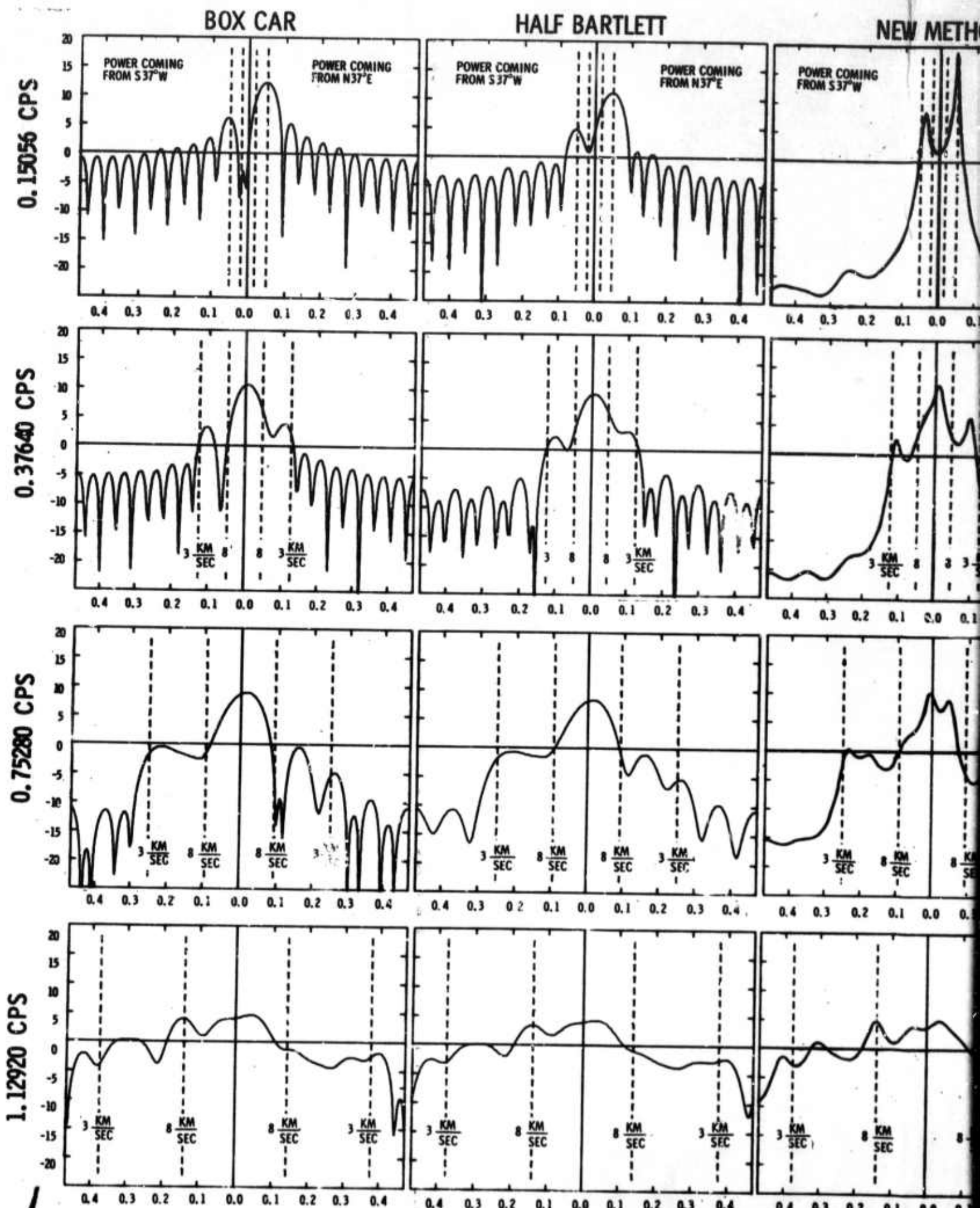
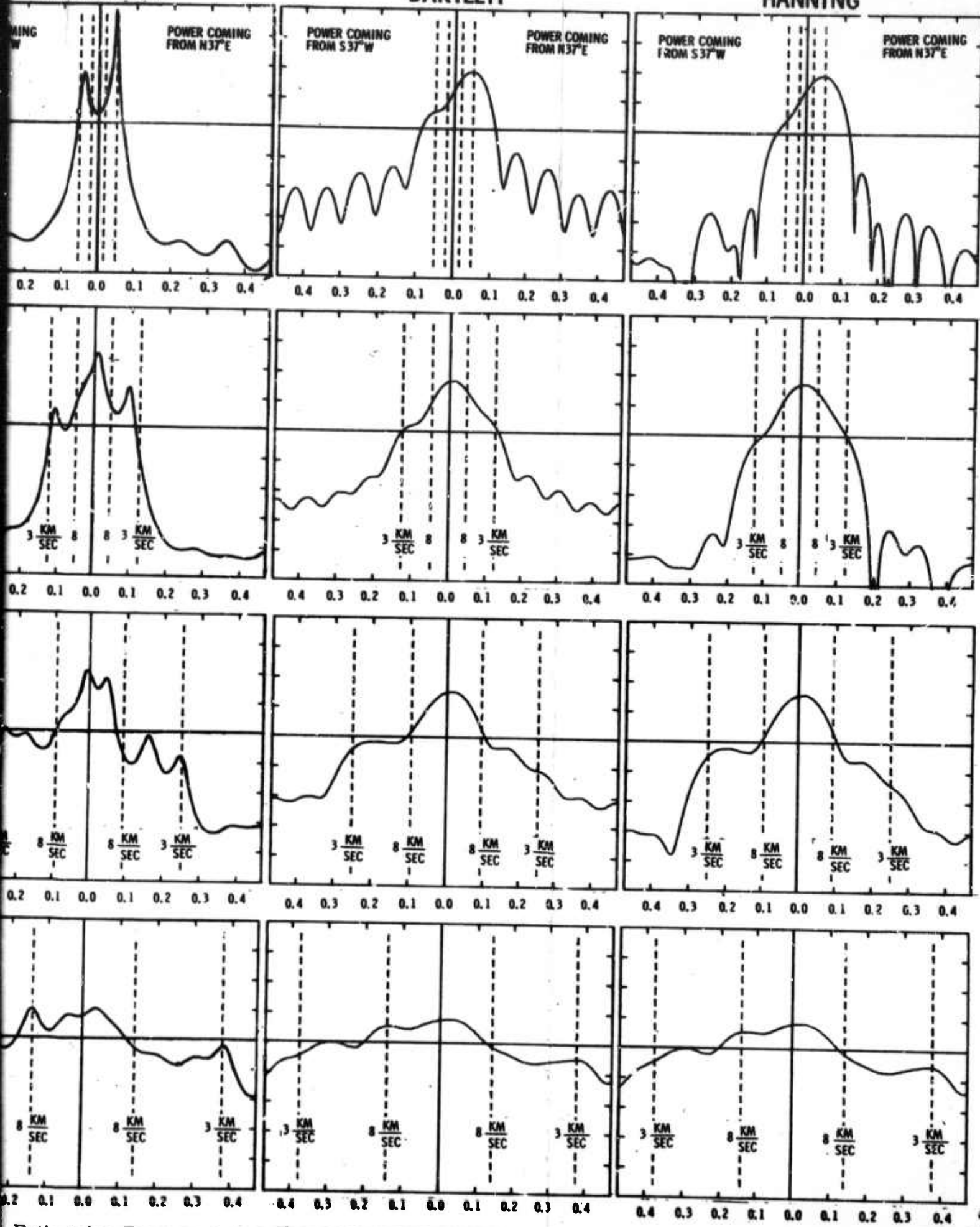


Figure 21. Comparison of the New Wavenumber Estimation

## NEW METHOD

## BARTLETT

## HANNING



Estimation Technique with More Conventional Techniques

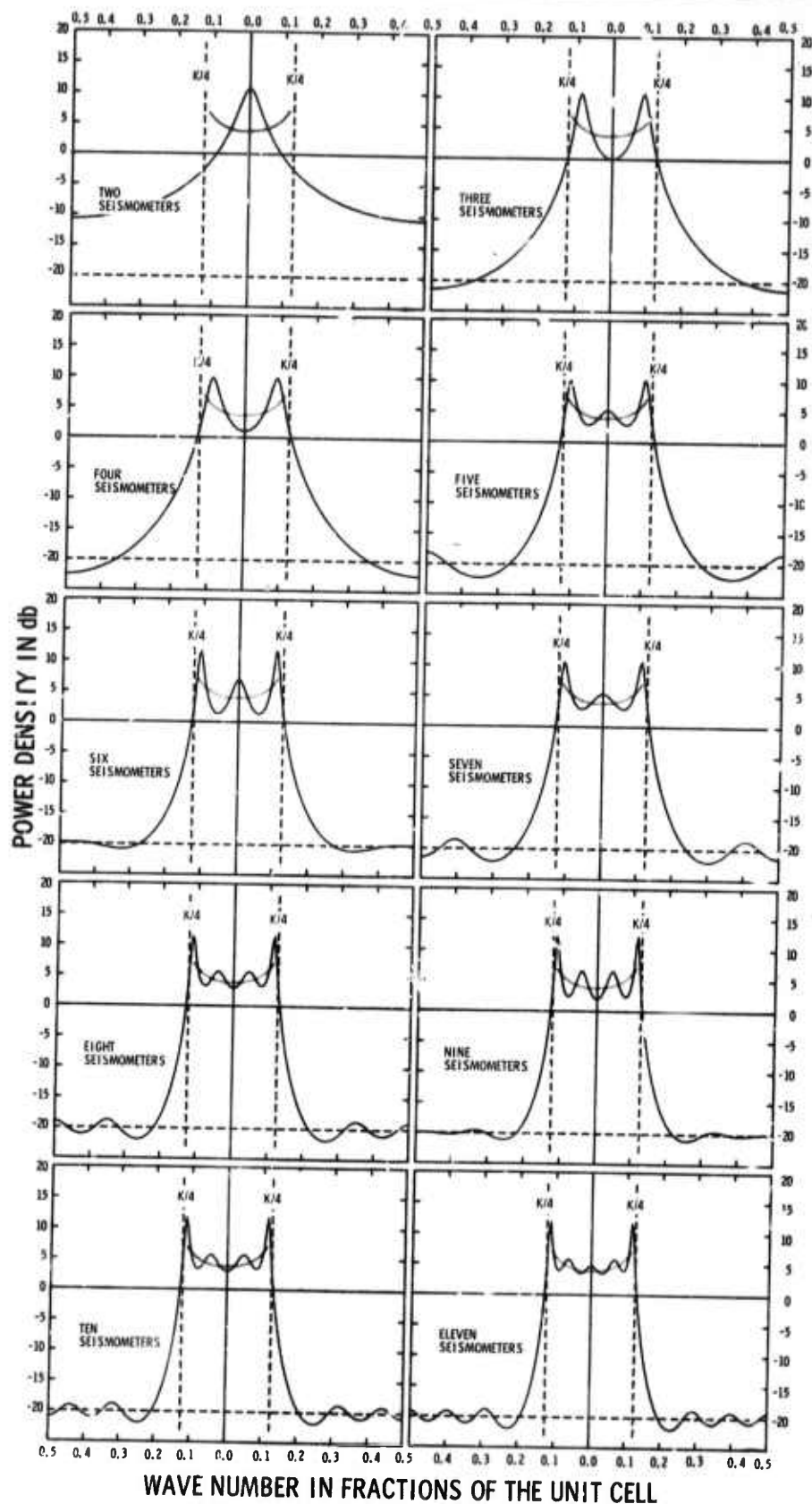


Figure 22. Approximations of the  $K/4$  Fixed Speed, Isotropic Model as a Function of the Number of Seismometers

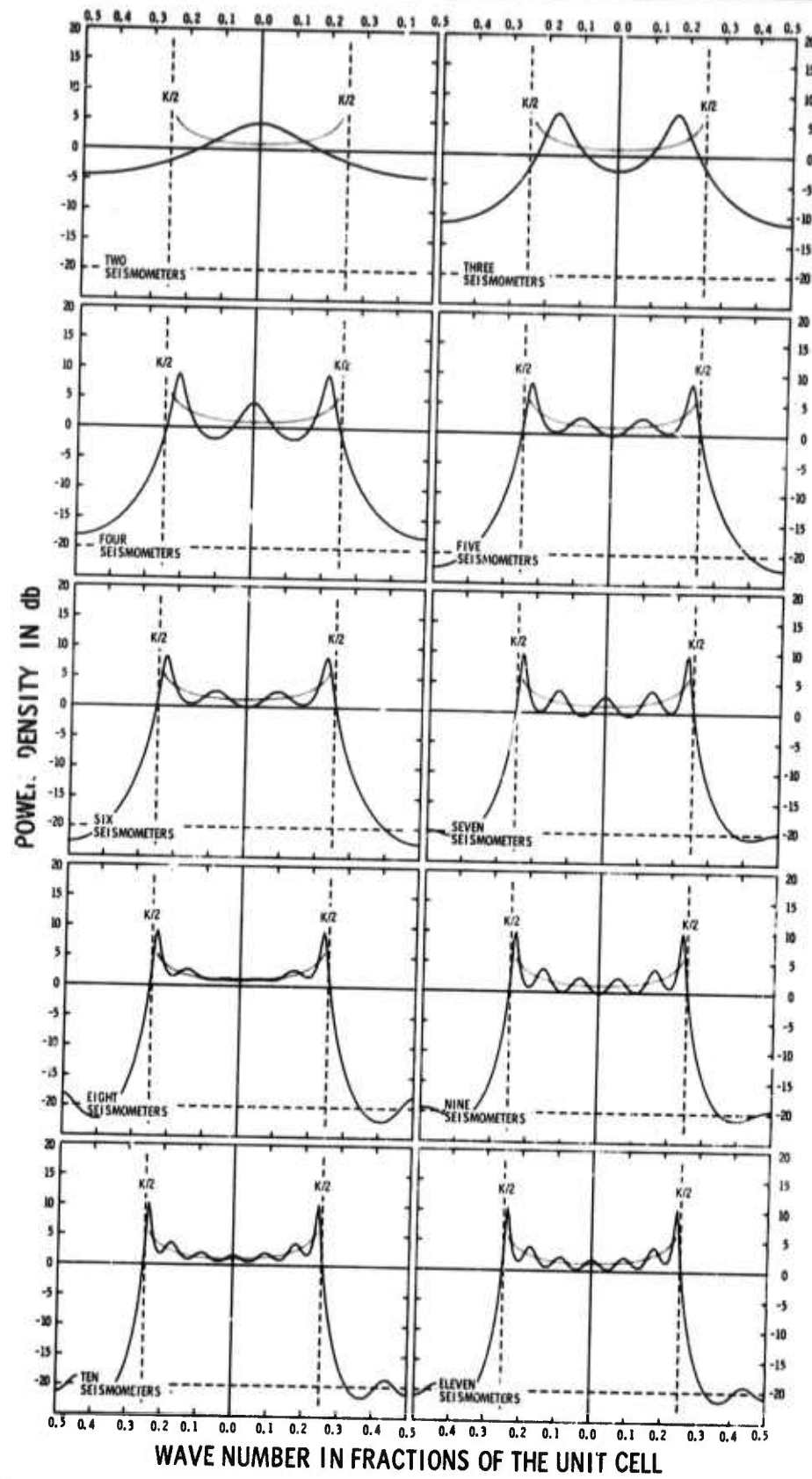


Figure 23. Approximations of the K/2 Fixed Speed, Isotropic Model as a Function of the Number of Seismometers

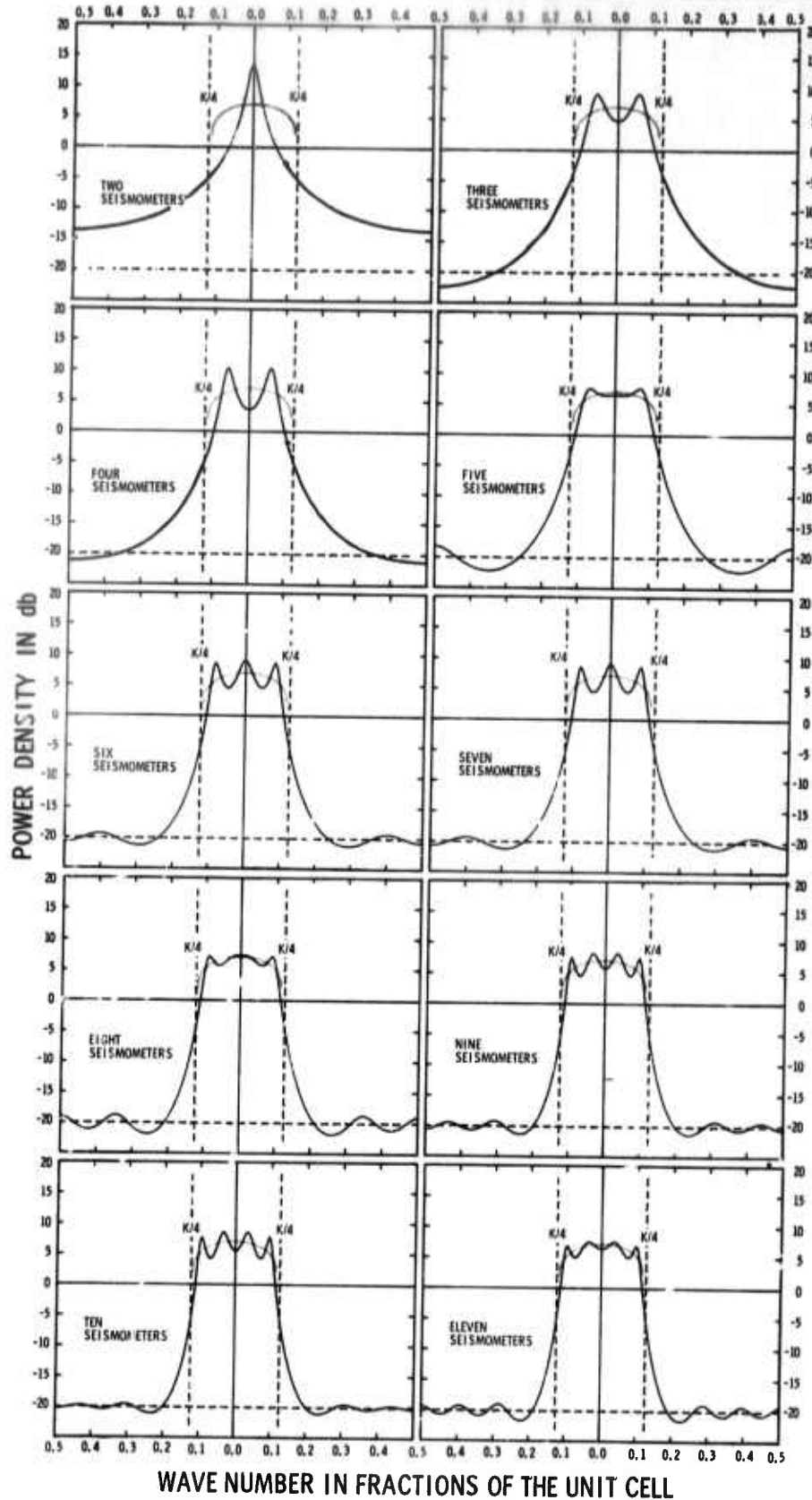


Figure 24. Approximations of the K/4 Solid Disk Model as a Function of the Number of Seismometers

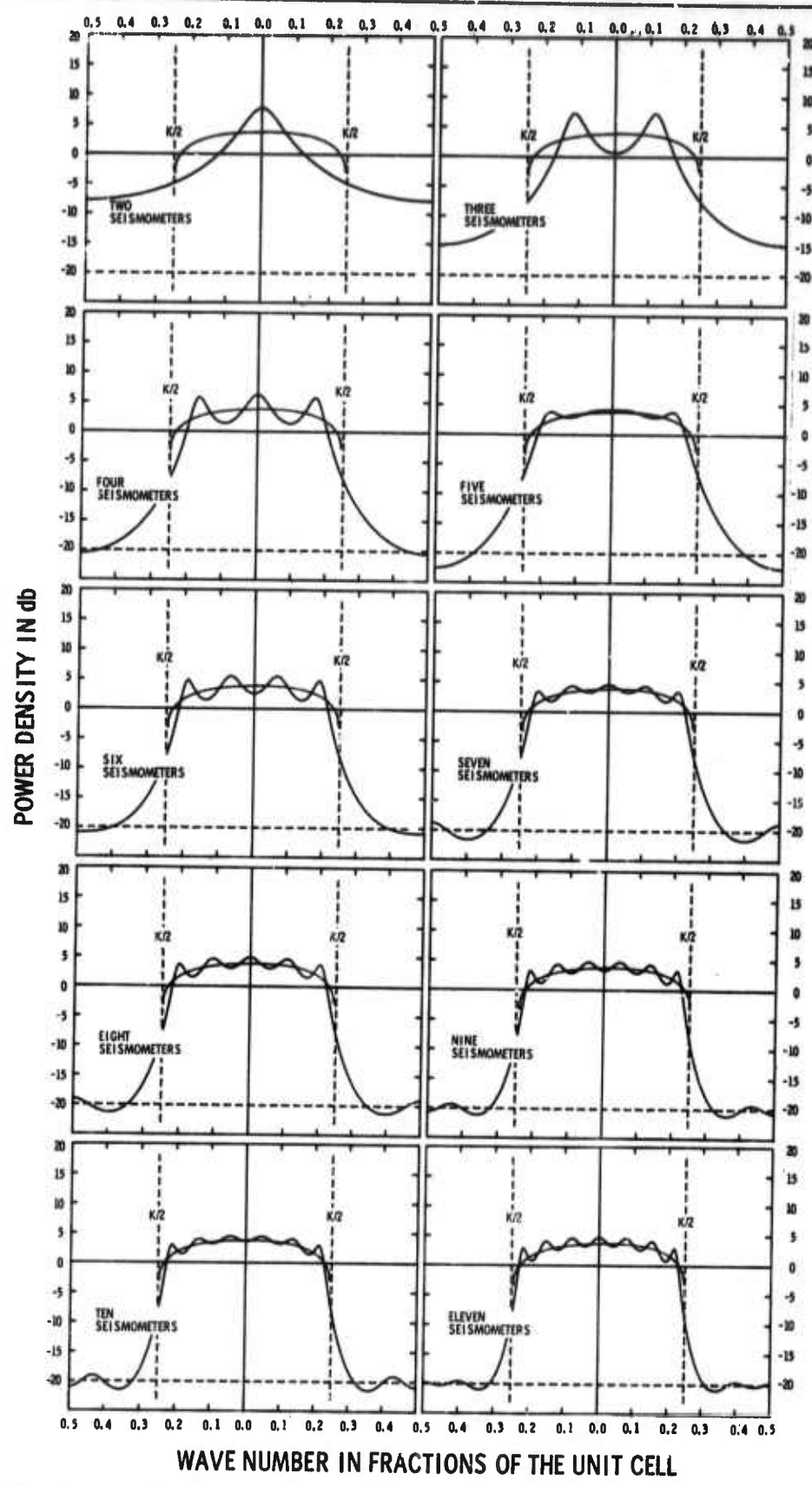
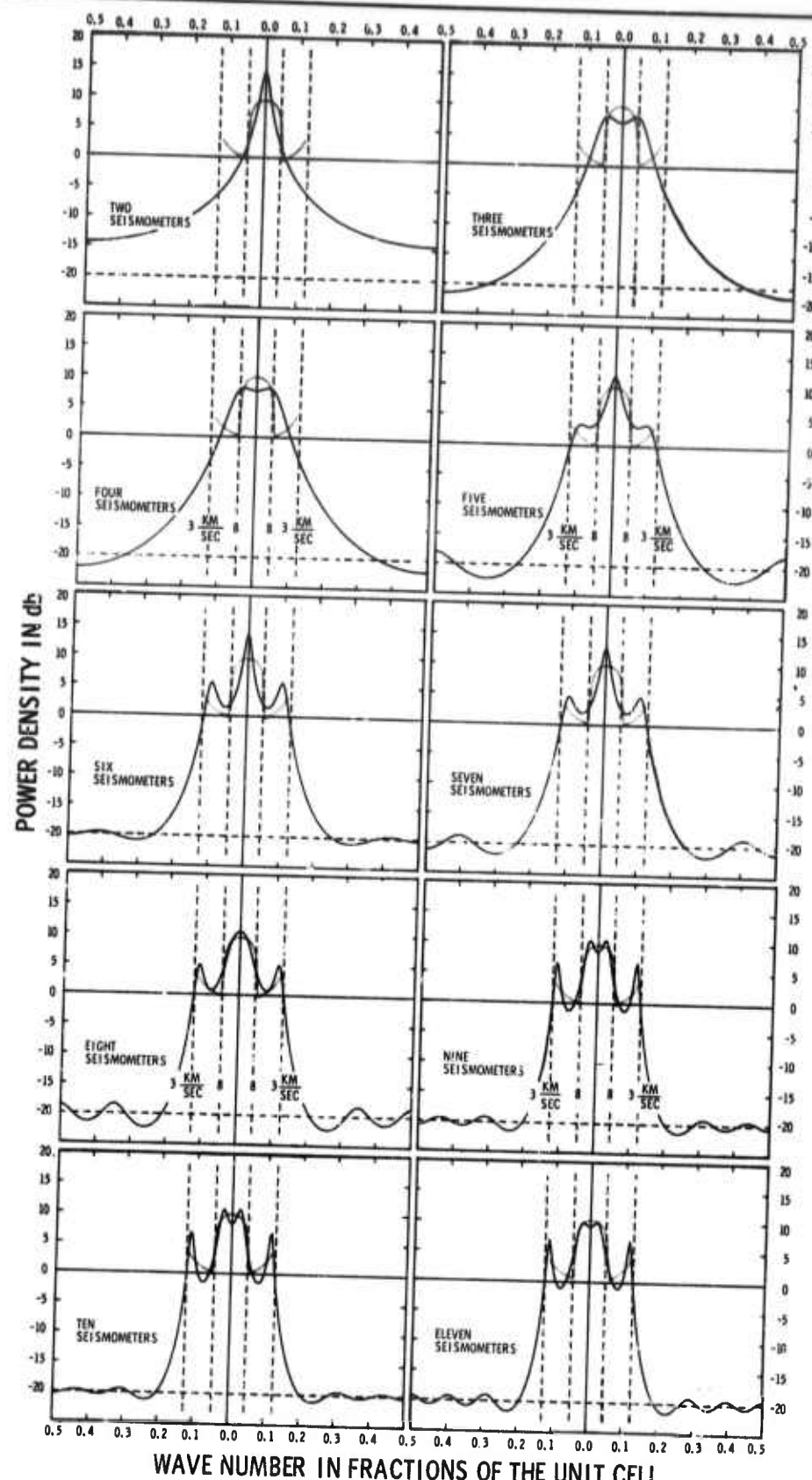


Figure 25. Approximations of the  $K/2$  Solid Disk Model as a Function of the Number of Seismometers



WAVE NUMBER IN FRACTIONS OF THE UNIT CELL

Figure 26. Approximations of the TFO 0.37640 cps Model as a Function of the Number of Seismometers

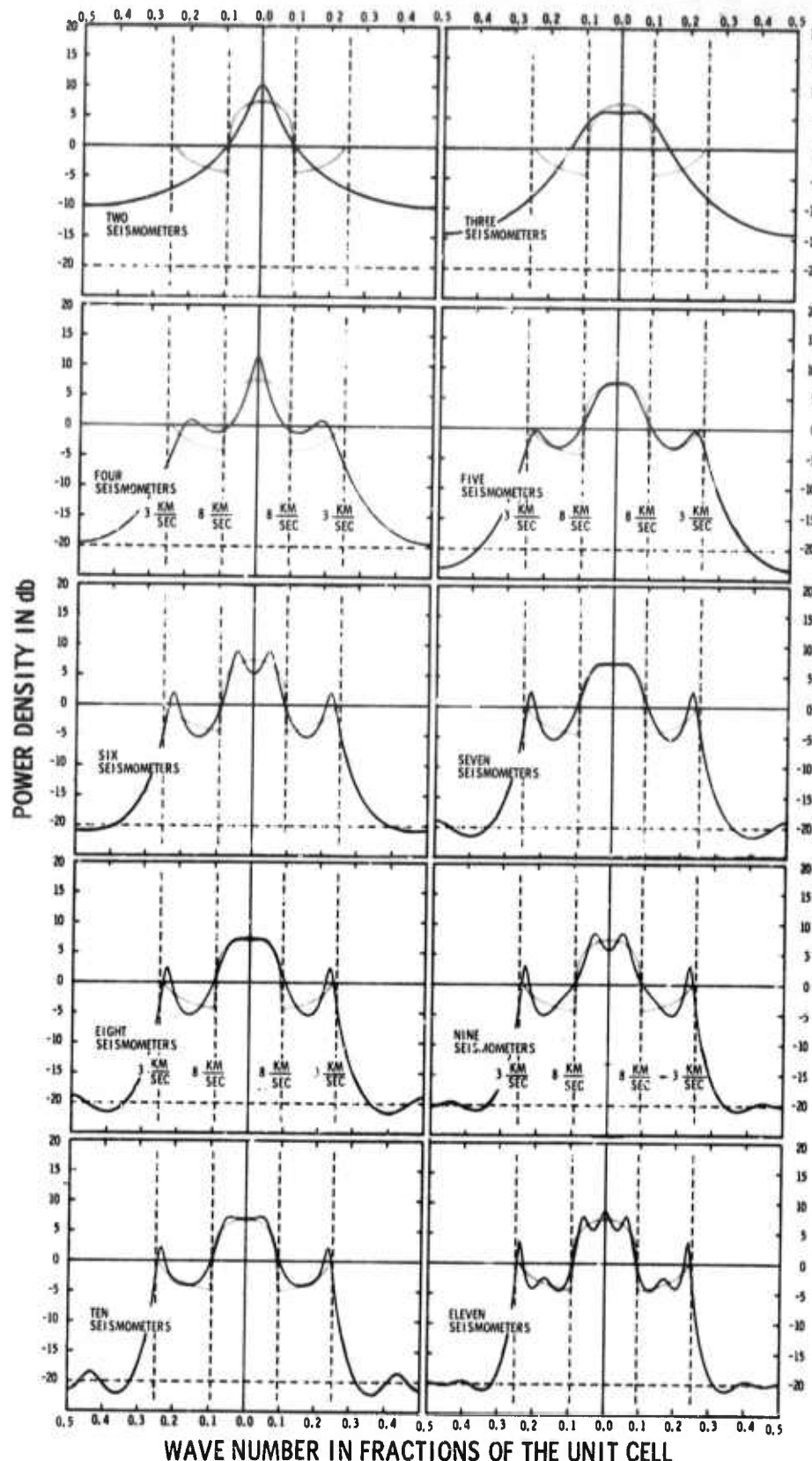


Figure 27. Approximations of the TFO 0.75280 cps Model as a Function of the Number of Seismometers



where  $M$  is the reciprocal wavelength of the propagation. In Figure 22,  $M$  is  $0.25K$ , the foldover wavenumber, and in Figure 23,  $M$  is  $0.50K$ . In both cases, a white or random noise equal to 1 percent of the total noise has been added to the models. This noise level is indicated by the -20 db dashed line.

In Figures 24 and 25, approximations to the solid disk model are investigated. The projection of this model onto a line has the mathematical form

$$P(k) = \frac{2 \sqrt{M^2 - k^2}}{\pi M^2} \quad \text{for } |k| \leq M$$

and

$$P(k) = 0 \quad \text{for } |k| > M$$

where  $M$  is the wavenumber corresponding to the edge of the disk. Figure 24 is for  $M$  equal to  $K/4$  and Figure 25 is for  $K/2$ , with 1 percent white noise being added to both models.

The model used in Figure 26 was made to approximate the wavenumber spectrum of the TFO long noise sample at 0.37640 cps. The theoretical spectrum, shown in the background of each plot, is a combination of the solid disk model (with about 63 percent of the power and an edge wavenumber of 0.047 cycles/km) and the fixed speed isotropic model (with about 36 percent of the power and a propagation wavenumber of 0.1255 cycles/km), together with 1 percent white noise. Figure 27 models the TFO spectrum at 0.75280 cps. In this case, the solid disk had about 73 percent of the power and an edge wavenumber of 0.094 cycles/km. The



---

fixed speed isotropic model had 26 percent of the power and a propagation wavenumber of 0.251 cycles/km and 1 percent white noise was added.

Figure 28 shows how well the theoretical 11-seismometer spectral estimations model the TFO wavenumber spectra at 0.37640 cps and 0.75280 cps. The TFO spectra and their integrated spectra for both arms of the array are shown in the foreground of the figure with the background containing the corresponding plots from the theoretical models of Figure 27 and 28.

The third investigation into the properties of this new wave-number estimation technique was directed toward obtaining an idea of how many seismometers in a line are needed in order to obtain adequate wave-number estimates. To do this, wavenumber spectra were generated as if there were only two seismometers, then three and so on up to the full 11 seismometers in the S37°W to N37°E line, starting from the S37°W end. For example, the top left-hand plot in each of the Figures 29 through 32 uses only data obtained from the southern most two seismometers in the S37°W-N37°E line. The top right-hand plots use information from only the southern most three seismometers. The bottom right-hand plots are the same as those given in previous figures. The four figures, 29 through 32, give these estimates for the frequencies of 0.15056 cps, 0.37640 cps, 0.75280 cps, and 1.1292 cps, respectively.

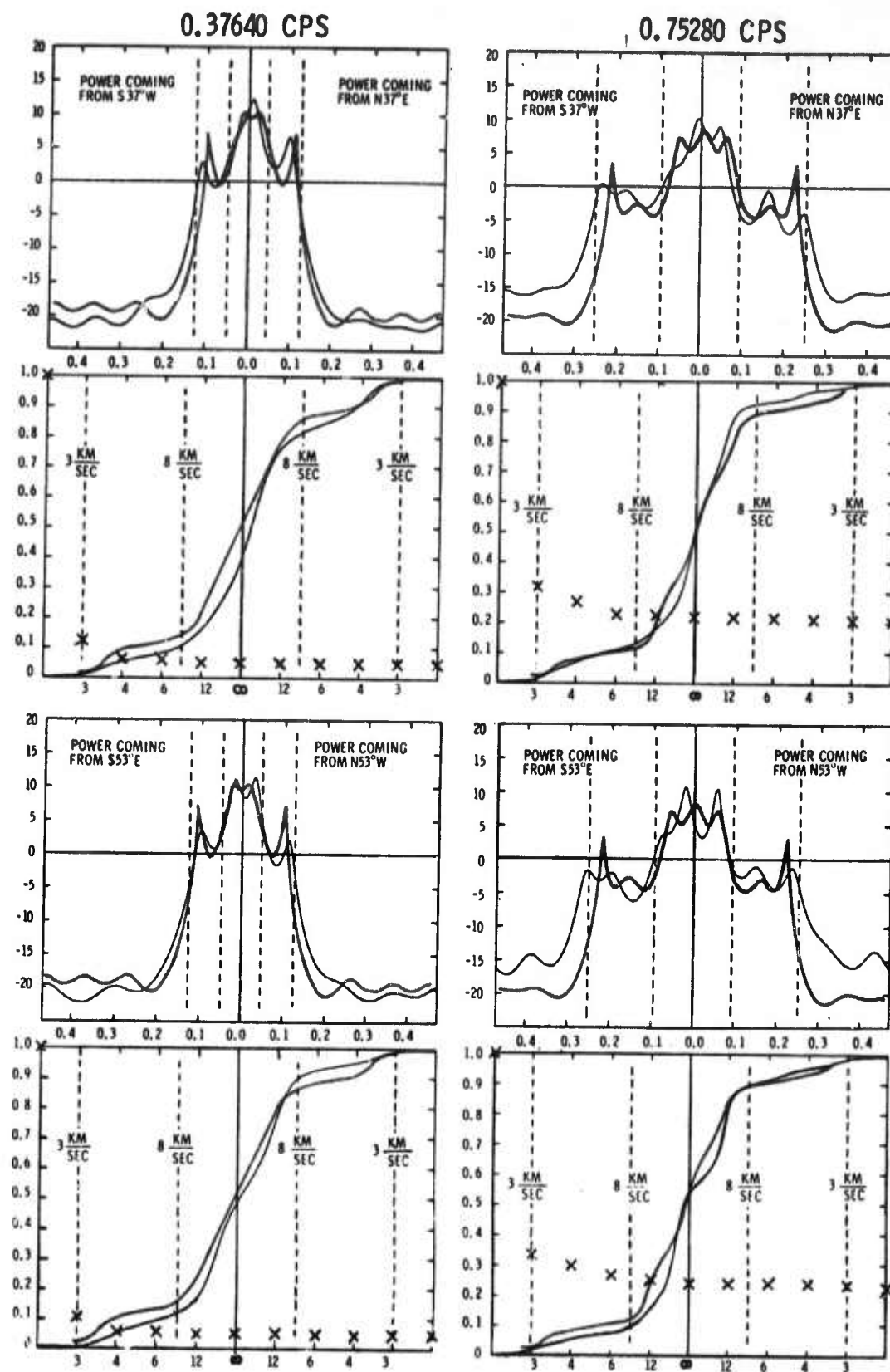


Figure 28. Comparison of Wavenumber Spectra at 0.37640 cps and 0.75280 cps with Theoretical Models

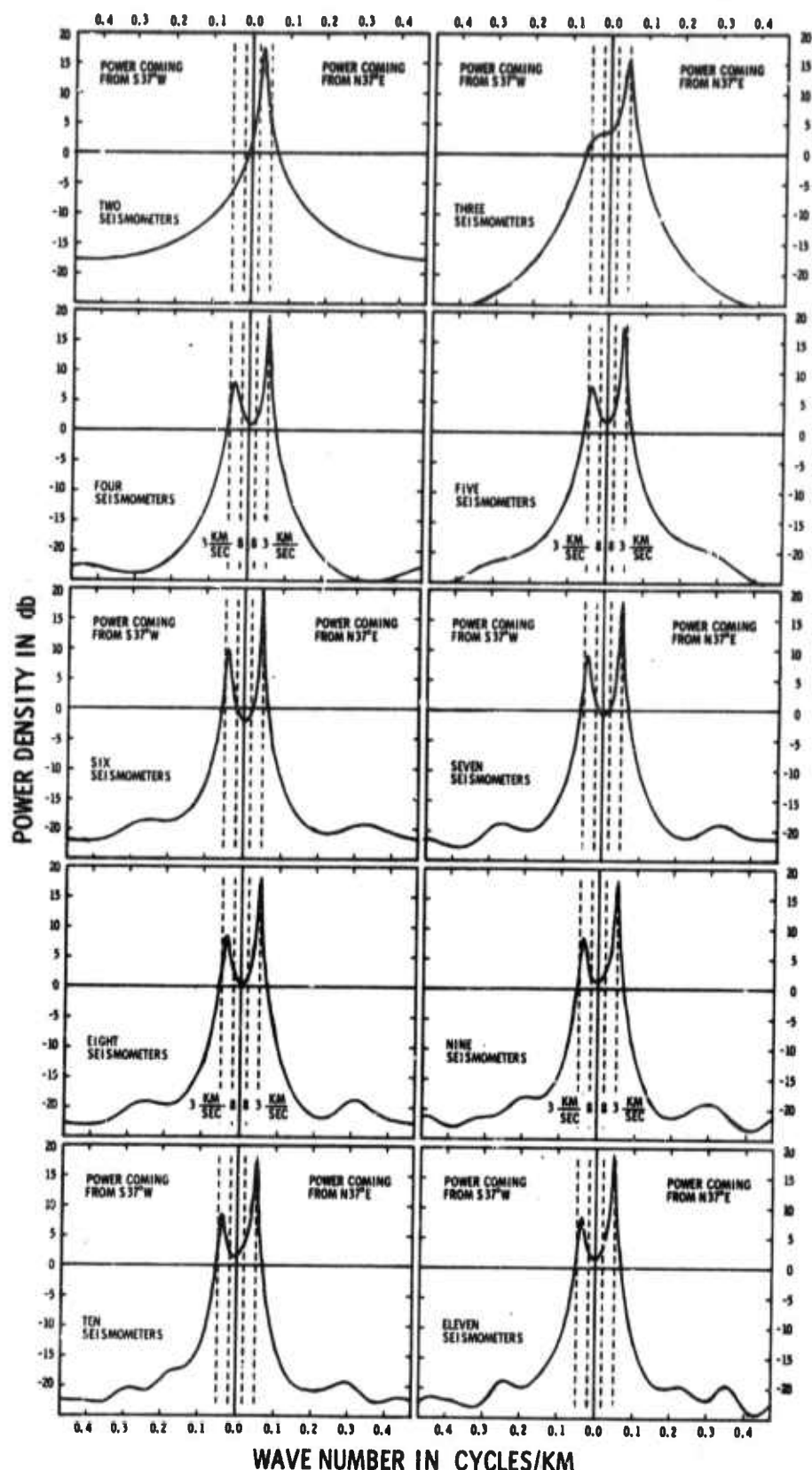


Figure 29. Estimated Wavenumber Spectra at 0.15056 cps as a Function of the Number of Seismometers

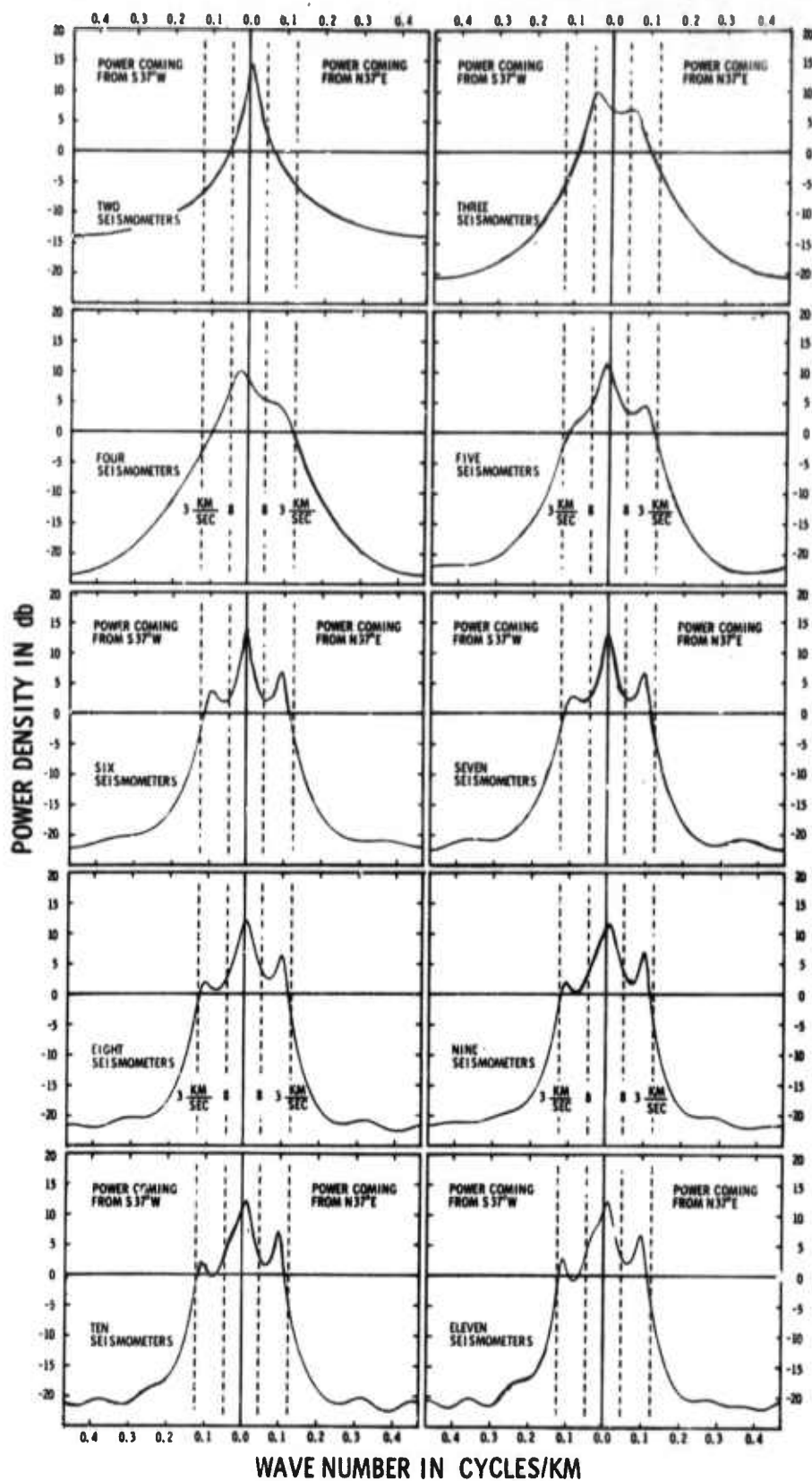


Figure 30. Estimated Wavenumber Spectra at 0.37640 cps as a Function of the Number of Seismometers

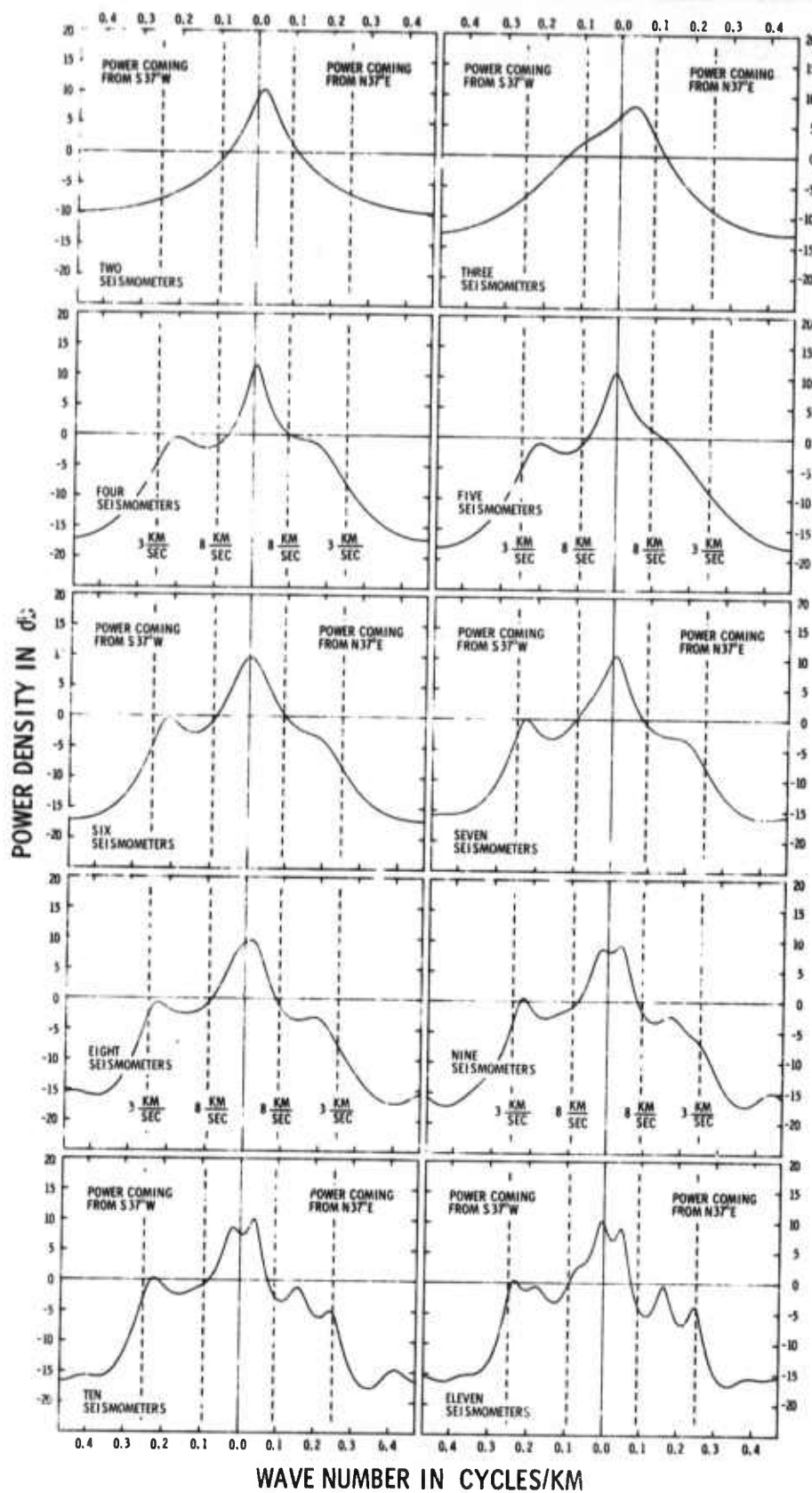


Figure 31. Estimated Wavenumber Spectra at 0.75280 cps as a Function of the Number of Seismometers

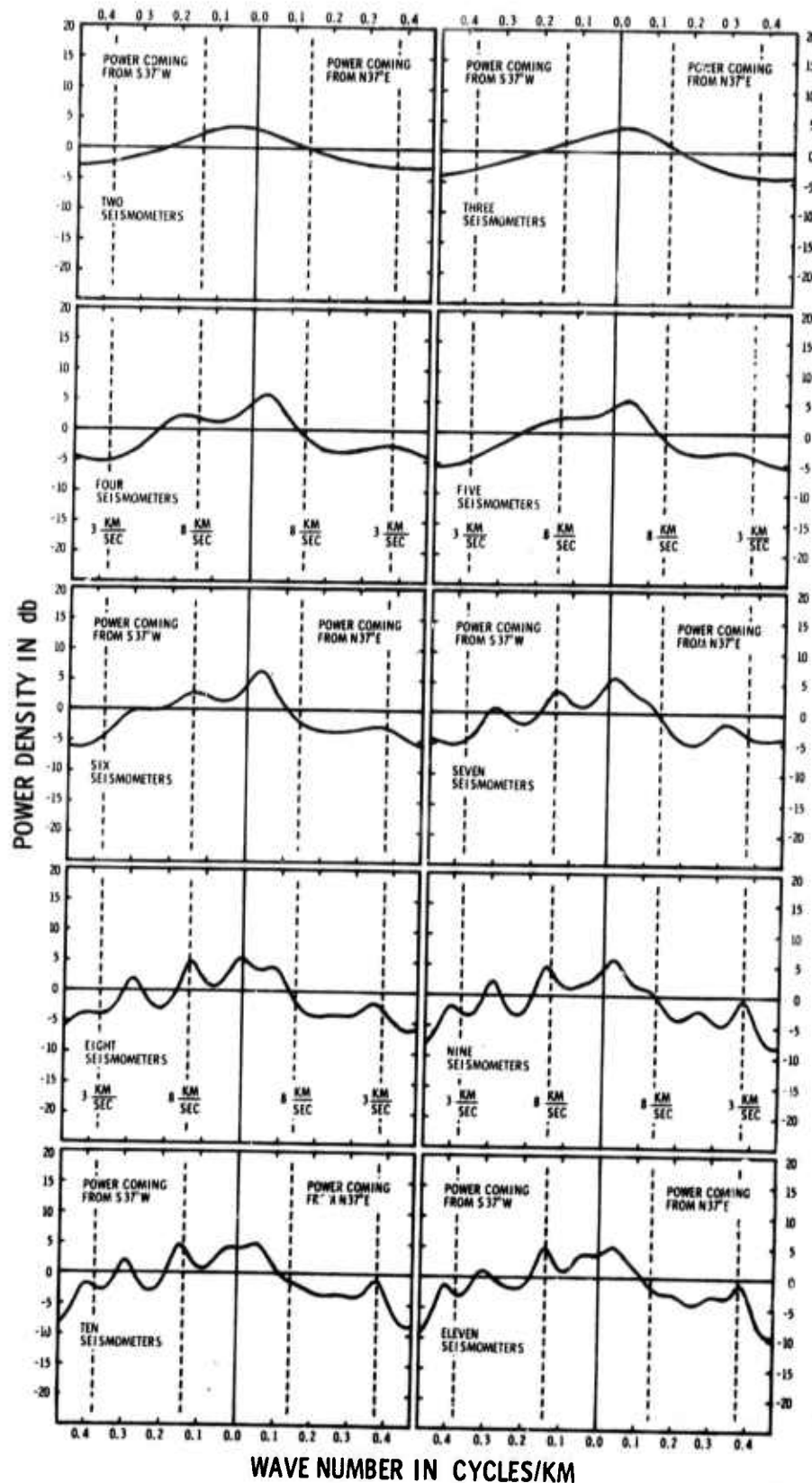


Figure 32. Estimated Wavenumber Spectra at 1.1292 cps as a Function of the Number of Seismometers



---

SECTION X  
REFERENCES

1. Texas Instruments Incorporated, 1965: Array Research Semiannual Tech. Rpt. No. 3, Contract AF 33(657)-12747, 3 Jun.
2. Texas Instruments Incorporated, 1966: Wavenumber Analysis of TFO Long-Noise Sample, Array Research Spec. Rpt. No. 17, Contract AF 33(657)-12747, 15 Sept.
3. Texas Instruments Incorporated, 1964: Multichannel Filter Systems for Tonto Forrest Observatory, Array Research Spec. Rpt. No. 2, Contract AF 33(657)-12747, 1 Sept.